Investigating Alginate Loading and Release For Controlled Payload Delivery Applications

by

Ryann Chatfield

A thesis submitted to the Faculty of the University of Delaware in partial fulfillment of the requirements for the degree of Honors Bachelor of Biomedical Engineering with Distinction

Spring 2026

© 2026 Ryann Chatfield
All Rights Reserved

Investigating Alginate

Loading and Release

For Controlled Payload

Delivery Applications

by

Ryann Chatfield

Approved: _____

Jason Gleghorn, PhD
Professor in charge of thesis on behalf of the Advisory Committee

Approved: _____

Ryan Zurakowski, PhD
Committee member from the Department of Biomedical Engineering

Approved: _____

Matthew Decamp, PhD
Committee member from the Board of Senior Thesis Readers

Approved: _____

Michael Chajes, Ph.D.
Dean, Honors College

ACKNOWLEDGMENTS

I want to thank Dr. Jason Gleghorn, my research advisor, for his guidance, support, and mentorship throughout the last three years. I am very grateful for the opportunities he has given me and the knowledge I have gained throughout my time doing undergraduate research. I have developed a passion for translational research, which sparked my interest in medicine, as well as my interest in drug delivery and immunoengineering. I also want to thank my post-doc and graduate student mentors, Dr. Michael Donzanti and Luisa Fink, who have helped me grow as an independent researcher and provided a great deal of guidance throughout this process. Lastly, I want to thank my friends and family for always believing in me and supporting me.

TABLE OF CONTENTS

LIST OF TABLES vi
LIST OF FIGURES vii
ABSTRACT ix

1 INTRODUCTION 1

1.1 Overview and Motivation 1

1.1.1 Lymph Node Metastasis Background and Physiology 1
1.1.2 Metastatic Cancer Mechanisms 4
1.1.3 Lymph Node Targeting 6
1.1.4 Current Treatment Strategies and Limitations 7
1.1.5 Microparticle Delivery Systems and Polymer Development 11

1.2 Objectives 13

2 Methods 16

2.1 Cell lines: 4T1 Cancer Cells 16
2.2 Alginate Prepolymer 16
2.3 Microparticle Droplet Generation: Flow-focusing Microfluidic Chip 17
2.4 Solvent Transfer/Particle Washing: Flow-focusing Microfluidic Chip 17
2.5 Microparticle Droplet Generation: Dropwise Emulsion Method 18
2.6 Solvent Transfer/Particle Washing: Dropwise Emulsion Method 18
2.7 Microparticle Stability 19
2.8 Particle Quantification (ImageJ) 19
2.9 Drug Loading 19
2.10 Loading Quantification 20
2.11 DOX Efficacy (Free Drug) 21
2.12 DOX Efficacy (Free versus Loaded) 21
2.13 DOX Efficacy Post Encapsulation (Varied Crosslinking) 22
2.14 Alamar Blue Assay 22
2.15 Statistical Analysis 22

3 Results 23

3.1 Aim 1 23

3.1.1 Droplet Generation 23
3.1.2 Droplet Size Quantification between Batches 24
3.1.3 Droplet Size Quantification between Groups 26
3.1.4 Droplet Washing 27

3.1.5 Droplet Storage Conditions 28
3.1.6 Droplet Stability 28

3.2 Aim 2 31

3.2.1 Drug Mass and Loading Comparison 31
3.2.2 Doxorubicin Loading 32
3.2.3 Crosslinking Density and Loading Efficiency 33
3.2.4 Free DOX Efficacy on 4T1 Cells 34
3.2.5 DOX Efficacy Post-Encapsulation 35
3.2.6 DOX Treatment with Varying Crosslinking Densities 36

4 Discussion 39

4.1 Aim 1: Develop an alginate droplet generating protocol for monodispersed droplets and efficient solvent transfer 39
4.2 Aim 2: Determine payload functionality and release from the MPs along with how a material change will impact release 41

5 Limitations, Future Directions, & Conclusions 47

REFERENCES 52

LIST OF TABLES

Table 1. A pass is defined as a clear microparticle pellet formed and separated from the oil phase in the centrifuge tube……...27

Table 2. Loading efficiency of Fluorescein-dextran and Doxorubicin loaded microparticles…….…….……..31

LIST OF FIGURES

Figure 4. DOX standard curve for determining DOX-loading in microparticles. y = 4.3285x. with the y-intercept forced through 0,0. The high R^2 of 0.9978 indicates a strong linear relationship. 20

Figure 5. Schematic of droplet generation protocol for (A) microfluidic flow focusing chip and (B) dropwise emulsion methods. 23

Figure 6. Alginate microparticles generated using the (A) dropwise emulsion method at 700 rpm and (B) flow focusing microfluidic chip (20x magnification). 24

Figure 7. Average microparticle size among batches for those made at (A) 700 rpm: 65.61 µm ± 22.08 µm, 66.19 µm ± 33.10 µm, and 79.9 µm ± 49.35 µm in batches 1, 2, and 3, respectively, and (B) 1200 rpm: 57.05 µm ± 19.60 µm, 51.19 µm ± 19.20 µm, and 44.05 µm ± 25.05 µm in batches 1, 2, and 3, respectively (ns = no significance, n =3). 25

Figure 8. Average size of particles made using the dropwise emulsion method at 700 rpm (69.83 µm ± 34.83 µm) and at 1200 rpm (53.3 µm ± 24.4 µm), and the microfluidic chip (47.36 µm ± 5.36 µm,). (* $p < 0.05$, *** $p < 0.001$, n = 3). 26

Figure 9. Alginate microparticles stored in (A) DPBS with calcium and magnesium and (B) DPBS + calcium after 72 hours at 4 °C (20X magnification). 28

Figure 10. Microparticle diameter (µm) across days 1-5 and day 10 when stored in DPBS with calcium and magnesium at 4 °C. Day 1: 11.2 µm ± 4.7 µm, Day 2: 12.4 µm ± 3.5 µm, Day 3: 9.9 µm ± 3.5 µm, Day 4: 11.0 µm ± 3.6 µm, Day 6: 11.6 µm ± 3.4 µm, Day 10: 10.5 µm ± 3.3 µm (ns = not significant, n =3). 29

Figure 11. Total particle number in a 6.5 mL sample across days 1-5. Day 1: 1.58E13, Day 2: 1.63E13, Day 3: 2.03E13, Day 4: 1.85E13, Day 5: 1.24E13. (n =1). 30

Figure 11. Doxorubicin-loaded microparticles made using the (A) flow focusing chip and (B) dropwise emulsion method (20x magnification). 32

Figure 12. DOX loaded microparticles made using the dropwise emulsion method under (A) brightfield and (B) Cy5 far red channels, showcasing particle aggregation (20x magnification). 33

Figure 13. Loading efficiency of MPs made with 2% and 6% acetic acid (n = 1). The loading efficiency for MPs with 2% acetic acid is 45.03% and for 6% it is 44.62%. 34

Figure 14. Cell viability of 4T1 cells after being exposed to 0.25, 0.35, 0.5, and 1 mg/mL of DOX for 48 hours. The media + saline group had an average viability of 88.4 ± 6.1%, the 0.25 mg/mL DOX treatment group had a viability of 20.8 ± 2.1%, the 0.35 mg/mL treatment group had a viability of 17.2 ± 4.1%, the 0.5 mg/mL treatment group had a viability of 10.9 ± 3.2%, and the 1 mg/mL treatment group had a viability of 10.6 ± 1.7%. The media only control was treated as 100% cell viability baseline (n = 3, ns = not significant, * $p < 0.05$, **** $p < 0.0001$)..... 35

Figure 15. 4T1 cell viability after exposure to Doxorubicin (DOX) for 36 hours. The media only control served as a 100% viability baseline. 4T1 cells treated with free DOX had a cell viability of 39.2% ± 42.6%, and those treated with the released DOX had a viability of 36.5% ± 11.9%. The media + saline group also had a viability of 100% ± 7.7% (n=3; ns = not significant, *** $p < 0.001$)..... 36

Figure 16. 4T1 cell viability after exposure to Doxorubicin (DOX) for 48 hours. The media only control served as a 100% viability baseline. The 6% unloaded group had a 136 ± 11.7% viability, the 6% loaded 50 µL and 100 µL groups had viabilities of 39.2 ± 1.31% and 39.7 ± 1.87%, respectively. The 2% unloaded group had a viability of 128 ± 16.7%, while the 2% loaded 50 µL and 100 µL groups had viabilities of 39.9 ± 1.53% and 37.2 ± 1.15%, respectively. Free doxorubicin at 2% concentration resulted in a viability of 40.3 ± 1.23%, and free doxorubicin at 6% concentration resulted in a viability of 38.8 ± 0.069%. (n=3; ns = not significant, **** $p < 0.0001$)..... 38

ABSTRACT

One of the main challenges faced when trying to treat metastatic cancer is that disease can persist in specific locations in the body that show poor drug penetration, or pharmacological sanctuary sites. One such example is the lymph node, as many small-molecule drugs display poor uptake in the lymph node lobule. This phenomenon is important in the context of metastatic cancer, as it allows cancer cells to "hide" in the lymph node lobules, unaffected by chemotherapies or other cancer-targeting drugs.

One approach to targeting cancer cells in the lymph node is the use of Trojan horse delivery vehicles, where drug payloads are hidden in a cell-mimetic vehicle. Polymers, such as alginate, are often used to manufacture these delivery vehicles because of their biocompatibility and biodegradability, which enable the creation of a tailored drug delivery platform.

It was hypothesized that microfluidic techniques could be leveraged to optimize microparticle core fabrication, drug and molecule loading, and drug release onto 4T1 cancer cells. Alginate was used to create microparticles by incorporating synthetic strategies to improve stability and enable tuned release parameters. To investigate this hypothesis, two aims were established: (1) Develop an alginate droplet generating protocol for monodispersed droplets and efficient solvent transfer and (2) Determine payload functionality and release from the MPs along with how a material change will impact release.

To develop a reliable protocol for generating monodispersed alginate droplets with efficient solvent transfer, two fabrication approaches were evaluated: dropwise emulsion and flow-focusing microfluidics. The flow-focusing device demonstrated the narrowest size distribution; however, the dropwise emulsion method offers size

tunability and has a much higher throughput. Following several washing steps with octanol, PBS, and isopropanol, the microparticles were left completely in the aqueous phase. Additionally, storing the particles at 4 °C and in a buffer that contains calcium and magnesium helped maintain particle stability and prevent premature degradation by maintaining alginate crosslinks. This aim helped establish a robust droplet generation protocol, along with optimal washing and storage conditions.

To evaluate loading across molecules of different sizes, particles were encapsulated with 500 kDa FITC-dextran and Doxorubicin (DOX). Both molecules were successfully encapsulated with comparable loading efficiencies, indicating that molecules of significantly different sizes can be loaded. When particles made via the dropwise emulsion method were loaded with DOX in concentrations greater than 1 mg/mL, significant clumping and aggregation occurred; however, particles were still loaded with drug. When particles were crosslinked with 2% and 6% acetic acid, similar levels of DOX encapsulation were achieved under identical loading conditions.

To test the efficacy of DOX post-encapsulation and release, the efficacy of free DOX on 4T1 cells was first confirmed. After 48 hours, free DOX demonstrated a clear dose-dependent reduction in cell viability; however, the lack of statistical significance between the higher concentration groups (0.35 mg/mL, 0.5 mg/mL, and 1 mg/mL), suggests that maximal cytotoxicity is reached at relatively low DOX concentrations. To then confirm that DOX remains effective after encapsulation, microparticles were incubated in saline to allow DOX release, and the resulting DOX-containing saline was applied to 4T1 cells. It was found that cells treated with free DOX had a viability comparable to that of the free DOX treatment group at the same concentration. Lastly, particles crosslinked with both 2% and 6% acetic acid were

loaded with DOX and placed with 4T1 cells. After 48 hours, the cell viability in all DOX treatment groups showed no significant differences from each other but were different from that of unloaded particles. This aim helped demonstrate that DOX remains functional post encapsulation and that unloaded particles have no negative impacts on cell viability, while showcasing that a small (4%) change in acetic acid concentration does not impact loading or release.

This study showcased that this alginate microparticle platform is a robust and adaptable system for drug delivery, capable of encapsulating diverse molecules while preserving therapeutic efficacy. This work highlights the potential of emulsion and microfluidic fabrication techniques for designing tunable and effective drug delivery systems for cancer therapy and potential lymph node targeting downstream.

Chapter 1

INTRODUCTION

1.1 Overview and Motivation

1.1.1 Lymph Node Metastasis Background and Physiology

One of the main challenges faced when trying to treat metastatic cancer is that disease is able to persist in specific locations in the body that show poor drug penetration, or pharmacological sanctuary sites. One such example is the lymph node, as many small-molecule drugs display poor uptake in the lymph node lobule. This phenomenon is important in the context of metastatic cancer, as it allows cancer cells to "hide" in the lymph node lobules, unaffected by chemotherapies or other cancer-targeting drugs. This sanctuary effect arises in part from the unique transport architecture of the lymph node, including conduit and sinus networks that limit access of small molecules to the deeper parenchyma, and represents a barrier qualitatively analogous in its impact on drug delivery to the blood-brain and maternal-fetal placental barriers [1].

Lymph nodes have an associated artery or vein that terminates into a high endothelial venule (HEV), where trans-endothelial migration of circulating lymphocytes occurs [2]. Trans-endothelial migration refers to the movement of leukocytes across the endothelial lining of certain vessels. The major structures of the

lymph nodes include the capsule, the subcapsular sinus, the cortex, and the medulla. The capsule consists of dense connective tissue and collagenous fiber, which extend inside to form trabeculae. The subcapsular sinus is the space between the capsule and cortex, which allows lymphatic fluid to be transported. Found below the subcapsular sinus is the cortex, which is formed of the outer cortex and the paracortex. It contains quiescent lymphocytes, antigen-stimulated B-cells, and follicular dendritic cells [3]. The medulla is the innermost layer of the lymph node that contains large blood vessels, sinuses, and medullary cords. The medullary sinus drains lymph into efferent vessels. Together, the cortex, the paracortex, and the medulla make up the parenchyma, or lobule. Inside the parenchyma are the conduits, composed of fibroblastic reticular cells supported by a network of collagen fibers that allow a portion of the lymph deeper access to the lymph node parenchyma. The conduits allow the lymph and some small molecules to be delivered to the high endothelial venules (HEVs), the specialized areas of lymph nodes that facilitate the movement of lymph back into the lymph nodes from the blood at a steady state.

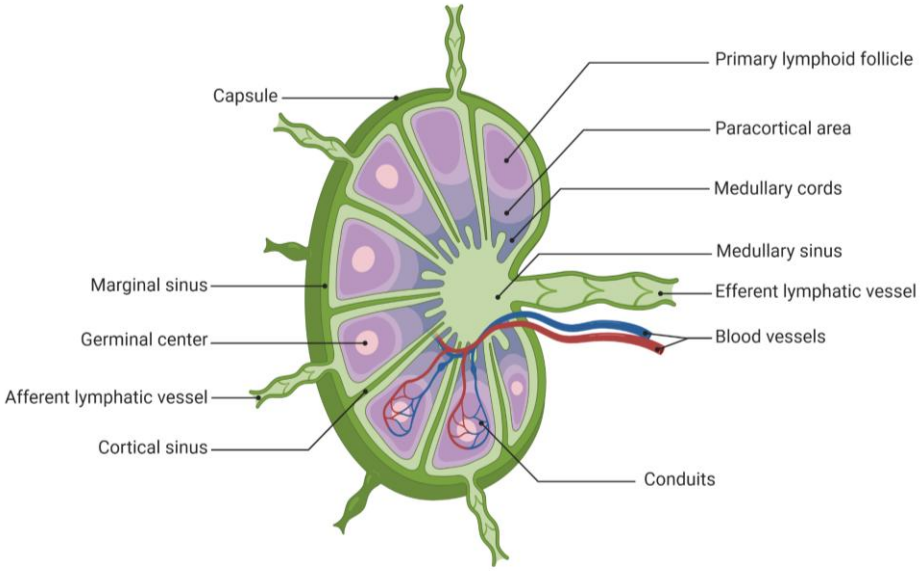

Figure 1. Schematic of a lymph node.

Although they act as a line of defense for the body, lymph nodes also provide a major pathway for primary tumors to metastasize because the lobules offer a safe space for tumor cells to persist without therapeutic levels of chemotherapeutic drugs (Figure 1) [4]. Because lymph nodes filter foreign material, they are frequently the first destination for cancer cells spreading through the lymphatic system. Recent work has developed accessible workflows for high-fidelity 3D anatomical reconstruction of the murine lymph node, including lobules, conduits, and high endothelial venules, providing the geometric framework needed for spatial pharmacokinetic modeling of LN-targeted therapeutics [5].

1.1.2 Metastatic Cancer Mechanisms

Lymph node metastasis occurs when there is a loss of cell-to-cell adhesion, allowing cancer cells to break away from the primary tumor and travel through the lymphatic system to the lymph nodes. E-cadherin junctions transmit measurable mechanical tension between epithelial cells, and disruption of these junctional forces, whether by mutation, mechanical stress redistribution, or loss of intercellular contractility coupling, directly contributes to epithelial-mesenchymal transition and the invasive phenotype that initiates lymphatic dissemination [6]. Likewise, malignant tumors have been known to produce growth factors, such as VEGF-C and VEGF-D, which induce lymphangiogenesis [7]. Vascular sprouting in response to growth factor cues is a sex-dependent process, with male and female endothelial cells exhibiting differences in sprouting rate, directionality, and metabolic priming, variability that is increasingly recognized as relevant to tumor-induced lymphangiogenesis and to the design of pre-clinical models of LN delivery [8, 9]. This increases lymphatic vessel density and improves tumor drainage, creating more routes for cancer cells to travel from the primary tumor to tumor-draining lymph nodes. Engineered three-dimensional vascular networks reconstituted from primary endothelial cells provide a tractable in vitro framework for studying how tumor-derived factors remodel sprouting behavior, network density, and the perfusable architecture that governs cell trafficking out of the primary tumor [10], [11]. Increased pressure within the tumor and changes in cell adhesion also make it easier for tumor cells to detach and migrate [12]. Once inside the

lymphatic system, the cells are transported with lymph fluid to regional lymph nodes, where they begin to multiply.

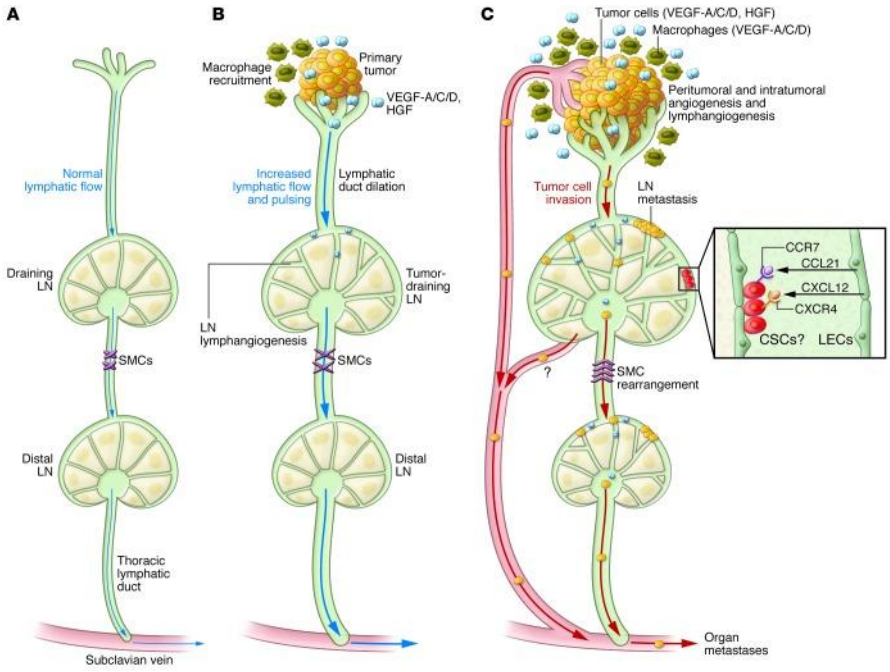

Figure 2. Schematic of lymph node metastasis mechanisms [12].

Once the cancer cells reach the lymph nodes, they can shift the phenotype and quantity of immune cells present in the lymph nodes. More specifically, they often make it so there are fewer cancer-killing immune cells and more T-regulatory cells. Although T-regulatory cells typically suppress excessive immune responses to protect healthy cells from being attacked by other immune cells, they have been known to play a role in inhibiting antitumor immunity and can even be programmed to protect the tumor. Metastatic cancer cells in lymph nodes also tend to have higher levels of PD-L1 and MHC-1, proteins that prevent immune cells from attacking cancer cells

[13]. As a result, the cancer cells are able to evade natural killer (NK) and other immune cells.

The promotion of immune tolerance and priming of distal sites by the release of pro-tumor soluble factors back into systemic circulation significantly decreases the likelihood that immune cells will attack the cancer cells as they travel throughout the body, allowing the cancer to spread [13]. By upregulating immunosuppressive proteins, cancer cells can effectively suppress local immune responses within the lymph node microenvironment, allowing them to survive, proliferate, and establish metastatic colonies without being eliminated by the host's immune system [14]. In addition to treating lymph node-resident disease, technologies for lymph node-targeted delivery are needed for enhancing immune responses and improving the efficacy of cancer immunotherapies.

1.1.3 Lymph Node Targeting

Beyond its well-established role in cancer metastasis, the lymph node is a relevant therapeutic target across a wide range of biomedical applications due to its central function in coordinating immune responses. In immunotherapy, lymph nodes serve as primary sites for antigen presentation and T-cell activation, making them critical for enhancing anti-tumor immunity [15]. Similarly, in vaccine development, targeted delivery to lymph nodes can improve antigen recognition and the generation of robust, long-lasting adaptive immune responses, which is especially important for subunit and mRNA vaccines [16]. Lymph nodes are also key reservoirs in infectious

diseases, particularly in HIV, where the virus can persist within lymphoid tissue despite antiretroviral therapy, posing a major barrier to eradication [17]. Together, these applications highlight the lymph node's importance as a site for enhancing and regulating immune function, showcasing the broader translational potential of technologies designed to access and modulate this immune hub. A recent comparative analysis of physiological barrier drug delivery further identifies the lymph node as a clinically underdeveloped target relative to the blood-brain barrier, with only a small number of active LN-targeted delivery trials, the majority in oncology, establishing both the unmet need and the translational opportunity for LN-targeted microparticle systems [1].

1.1.4 Current Treatment Strategies and Limitations

Treatment of metastatic cancer is complex, as the cancer is found in several locations throughout the body, and it is challenging to reach cancer cells in the lymph nodes to prevent further metastasis. Additionally, metastatic cancer cells can be difficult to detect and are often located in an immunosuppressive environment. Current treatments for metastatic cancer include chemotherapy, a systemic approach that uses drugs to destroy rapidly dividing cancer cells [18]; hormone therapy, which blocks or reduces the hormones that certain cancers rely on for growth; immunotherapy, which enhances the body's immune system to recognize and attack cancer cells; radiation therapy, which uses high-energy radiation such as X-rays to kill cancer cells and is often combined with chemotherapy or surgery [19]; and targeted therapy, which interferes

with specific molecular pathways involved in cancer cell growth and proliferation [20]. However, treatment varies by individual and is based on cancer type and clinical presentation. With metastatic cancer in particular, there may be multiple lines of treatment depending on where the cancer has spread to.

The American Society of Clinical Oncology has published guidelines to provide a framework and aid in the treatment of many types of cancer, including breast cancer, melanoma, and thoracic cancer [21]. For advanced cancer, such as metastatic cancer, the goal of treatment may focus more on preventing the further spread of cancer, controlling tumor size, and extending a patient's life [22]. Some cancers are unresponsive to treatment, while some have a partial response or reappear later on. In particular, metastatic cancer is often resistant to therapies, which is the primary cause for overall treatment failure. Even if initial treatment is successful, there is the risk of cells evolving to evade therapies [23].

In recent years, new delivery systems have been developed to improve targeted drug delivery and increase overall therapeutic outcomes, including nanoparticle (NP) and cell-derived systems. NPs can target a drug directly to a tumor site, triggering the maximum drug release at a specific location. For example, the Trojan horse method is commonly used for NP delivery, which involves engineering nanoparticles for lymphatic uptake and delivery into the lymph nodes [24]. Membranes of red blood cells, leukocytes, cancer cells, NK cells, and platelets have been used to camouflage NPs [24]. This camouflaging leads to prolonged circulation and tumor targeting. Nanoparticle size, surface chemistry, and shape are dominant design parameters governing systemic

circulation, organ accumulation, and barrier penetration, with optimal sizes in the 10 to 100 nm range for systemic distribution and PEGylation as the canonical strategy for reducing hepatic clearance and prolonging circulation [25]. The protein corona that forms on nanoparticle surfaces upon contact with biological fluids is a critical determinant of circulation time, biodistribution, and cellular targeting fidelity, and engineered modulation of corona composition through PEGylation, self-peptide coating, or pre-adsorption with serum proteins can re-direct nanoparticle fate in ways that override the originally engineered surface chemistry [26]. For example, NPs covered in membranes made of both dendritic and cancer cell membranes had significantly higher lymph node homing ability than NPs not disguised. Red blood cell delivery is another method of therapeutic delivery, as therapeutic agents can be loaded into or attached to RBCs, allowing drugs to remain in the bloodstream and be released in a controlled manner [27]. This approach can improve drug stability, reduce toxicity, and enhance targeting.

That being said, these approaches still have limitations, including the fact that they can be toxic to some of the cellular components they interact with throughout the body. Nanoparticles tend to suffer from rapid clearance and off-target accumulation due to their size limitations. A study that aimed to quantify ligand-coated nanoparticle delivery to cancer cells in solid tumors found that only 0.7% of intravenously delivered nanoparticles trafficked to the tumor, and of those, only 0.0014% interacted with the cancer cells [28]. Direct in vivo biodistribution studies further demonstrate that nanoparticle accumulation is highly context-dependent, varying with surface chemistry,

dose, and host physiological state, and rigorous safety profiling across multiple organs is essential before translation [29]. These poor delivery efficiencies reflect inherent limitations of EPR-based passive targeting, where heterogeneous tumor vasculature, elevated interstitial fluid pressure, and rapid mononuclear phagocyte clearance constrain the therapeutic window for nanocarriers under approximately 100 nm in diameter [30].

Beyond nanoparticle systems, one of the most direct approaches for lymph node delivery is intranodal injection, in which therapeutics are delivered straight into the lymph node to maximize local exposure to antigen-presenting cells and lymphocytes. This method has been used in cancer vaccines and dendritic cell therapies to induce strong, localized immune responses due to immediate access to the lymph node microenvironment; however, it tends to be somewhat invasive, is technically difficult, and immunomodulatory agents are still cleared rapidly [31]. Peripheral administration routes, such as subcutaneous or intradermal injection, exploit natural lymphatic drainage, allowing molecules and cells to reach draining lymph nodes passively; however, small-molecule drugs still display poor lymph node retention and may leak into surrounding blood vessels.

Another method of treatment is antibody drug conjugates (ADCs). ADCs typically consist of a monoclonal antibody conjugated to a cytotoxic drug with a chemical linker [32]. Antibodies can be designed to target receptors expressed on dendritic cells, T cells, or HEVs, enhancing selective uptake and retention in lymphoid tissues following systemic administration. ADCs enable precise, cell-specific

targeting, making them particularly attractive for immunomodulatory therapies. That being said, ADCs face challenges such as off-target toxicity, premature payload release, and low efficacy [33]. As a result, there is a need for a new method that allows for successful tumor targeting and increased circulation time to deliver a therapeutic level of drug to the cancer cells. Lipid nanoparticle (LNP) systems offer a complementary platform that has matured rapidly for mRNA delivery and is capable of cell- and tissue-specific cargo delivery, including immunomodulatory cytokine mRNAs that locally reprogram the tissue microenvironment without systemic exposure [34]. Across maternal-fetal, oncologic, and immunologic disease contexts, nanomedicine platforms have repeatedly demonstrated that disease-tailored carrier design, combining site-specific targeting, tunable physiochemistry, and cargo protection, is required to translate efficacy from preclinical models to clinical use [35].

1.1.5 Microparticle Delivery Systems and Polymer Development

Polymers are widely used in the fabrication of drug delivery systems due to their tunable mechanical and chemical properties [36]. Both microfluidic techniques and traditional emulsion methods are commonly employed to process these materials into functional carriers [37]. The integration of polymers with microfluidics and emulsions enables the development of advanced delivery systems with precise control over structure and function.

Microfluidics involves the precise manipulation of small volumes of fluids within microscale channels, enabling highly controlled fabrication of polymer-based

systems [38]. In these devices, immiscible fluids can be combined to generate uniform droplets, forming the basis of emulsions. For example, water-in-oil or oil-in-water emulsions can be produced to encapsulate polymers and therapeutic agents [39]. By tuning flow rates, bath height, and fluid properties, microfluidic systems can generate monodisperse particles with consistent size and composition. These droplets can then be crosslinked to form microparticles or microgels. Microfluidic fabrication of alginate-based biomaterials enables sub-50 micrometer channel features and supports controlled, near-free-solution diffusion of both small molecules and macromolecules through the gel matrix, providing a precedent for using alginate as both a structural and transport-defining material in delivery applications [40]. Microfluidic device design for biomedical applications is a mature engineering discipline, with established design rules for transport-driven cell capture, particle sorting, and rare-cell isolation that translate directly to microparticle generation contexts [41-44].

Naturally derived polymers, such as alginate, are particularly advantageous in delivery systems due to their biocompatibility and biodegradability. These materials can be crosslinked to form stable networks through ionic interactions (e.g., calcium-induced crosslinking of alginate) or physical interactions like hydrogen bonding. Crosslinking controls properties such as stiffness, porosity, and degradation rate, all of which are critical for regulating drug release and cellular interactions. Together, microfluidics and polymers enable the creation of tailored drug delivery platforms, such as controlled-release particles and biomimetic systems for therapeutic applications. Photocrosslinked methacrylated alginate further enables decoupled tuning of stiffness, RGD-mediated

cell adhesion, and degradation rate, expanding the design space for cell-instructive and stimulus-responsive delivery vehicles. Layered alginate constructs can also be assembled by transient citrate chelation followed by re-crosslinking, providing a route to spatially heterogeneous architectures with controlled interfacial mechanics [45, 46]. Anatomically templated alginate constructs fabricated via injection molding from MRI- or micro-CT-derived geometries demonstrate that alginate hydrogels are compatible with patient-specific scaffold design, broadening the translational footprint of alginate as a delivery platform [47]. Recent advances combining bulk hydrogel-templating with self-assembled microvascular networks demonstrate that multiscale, serially perfusable constructs can be generated in a high-throughput manner, providing a route to in vitro testbeds in which microparticle release and tissue-scale transport can be evaluated together [48].

1.2 Objectives

The overall goal of this study was to optimize microparticle core fabrication, payload compounding, and drug release. The Gleghorn lab has focused on producing and characterizing T cell-mimetic microparticles for drug delivery. The microparticles use a “Trojan horse” strategy and target tissues, such as the lymph node, using their cell-mimicking properties to deliver small-molecule chemotherapeutics directly to the target tissue. In preliminary work, a cell-derived microparticle system that shows increased uptake in the lymph node has been developed. Because of their larger size, these microparticles are not cleared as rapidly by the kidneys, liver, and mononuclear

phagocyte system (MPS) [49]. This leads to an increased retention rate compared to NPs and a higher degree of delivery to the lymph node. This LN-resident delivery strategy aligns with a broader analysis of physiological barrier delivery, in which the lymph node is identified as a critical and underaddressed target compartment for both oncologic and immunomodulatory therapeutics [1]. However, this system still displayed poor loading and release kinetics. Moving forward, our objective is to continue iterating on this microparticle design by incorporating synthetic strategies to improve stability and enable tuned release parameters.

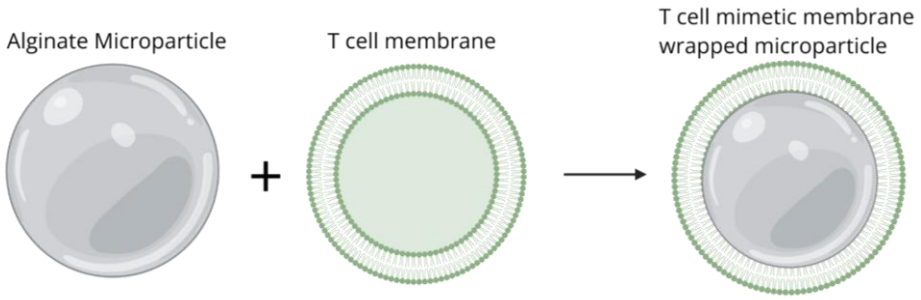

Figure 3. Schematic of T cell mimetic membrane wrapped microparticles (T3MP).

To develop and optimize a robust microfluidic protocol for generating monodispersed alginate droplets with efficient solvent transfer, key parameters, including flow rates, were tuned to achieve consistent droplet size and uniformity. The optimized protocol provides a reproducible method for producing uniform alginate-based MPs, enabling improved control over downstream applications such as drug delivery and therapeutic encapsulation. Complementary in vitro barrier models with

biochemically and biophysically tunable stromal compartments have also been developed in our group to enable controlled study of how carrier physicochemistry maps onto barrier-specific transport properties [50].

To investigate the loading kinetics of alginate MPs, their crosslinking density and size of loaded particles were varied. Loading parameters were assessed using fluorescent molecules. To test the efficacy of loaded molecules, loaded MPs were placed on 4T1s to determine whether the chemotherapies remained functional and could effectively target and kill cancer cells. An assay was run to assess cell viability after the cells were exposed to loaded MPs and chemotherapeutics for a set period of time.

The goals described above allow us to better understand if and how microparticle parameters can be changed to allow for tunable loading and release. It also allows us to determine how effective chemotherapy drugs are post-encapsulation, which can be applied to loading other molecules, such as antibodies, into MPs in future studies. The results have implications for the treatment of lymph node metastasis and other lymph node resident diseases.

Chapter 2

Methods

2.1 Cell lines: 4T1 Cancer Cells

The cell confluency was checked via brightfield microscopy (should be around ~80%). Media (RPMI 1640) was prepared by warming in a bead bath at 37 degrees C, and a warmed 0.25% trypsin aliquot was prepared. The old media was removed with a sterile aspirator, and the cells were rinsed with PBS. Three mLs of trypsin were added to detach cells from the plate and incubate for 5-10 minutes. Then 3 mL of complete media was added to the plate and pipetted up and down a few times to mix well. The cells were transferred to a separate tube and centrifuged for 6 minutes at RCF 200g at room temperature. The supernatant was removed and the pellet was resuspended in new media. Based on the cell count, the optimal amount of media needed to avoid overcrowding was determined. This volume was added to the plates, making sure cells were evenly distributed, and placed in incubator. For 4T1 cells, the typical subculture is between 1:6 and 1:8. The 4T1 line has been used in prior lab studies as a model invasive breast carcinoma in mechanically defined tissue contexts, supporting its use here as a relevant target for chemotherapeutic delivery [6].

2.2 Alginate Prepolymer

The alginate pre-polymer, typically 2% alginate, was made by putting 200 mg of alginic acid sodium salt and 281 mg of Calcium EDTA into 10 mLs of DI water. The vial containing the prepolymer sat on the rocker for 1 hour at room temperature or overnight at 4°C to completely dissolve the alginic acid and CaEDTA.

2.3 Microparticle Droplet Generation: Flow-focusing Microfluidic Chip

A 3mL syringe contains one or two percent alginate, while the other 10 mL syringe contains Novec 7300 oil + 2% Krytox (continuous phase). The alginate syringe was connected to the front channel of the microfluidic device, and the continuous phase was inserted into the back channel. The syringes containing the continuous phase and the alginate were pushed until one drop comes out. Both syringes were then attached to separate flow pumps. The flow pump with alginate was set to 0.05 mL/min, and the oil + Krytox syringe pump was set to 0.7 mL/min. As the syringes empty, the contents were collected in a 15 mL conical tube. Alginate particles were chelated using 2% acetic acid for 45 minutes. For every 2 mL of particles, 1 mL of acetic acid was added. The flow-focusing approach builds on a longstanding precedent in microfluidic alginate biomaterial fabrication, in which immiscible-phase shearing at lithographically defined junctions enables uniform droplet generation under tightly controlled hydrodynamic conditions [40, 51].

2.4 Solvent Transfer/Particle Washing: Flow-focusing Microfluidic Chip

After 45 minutes, acetic acid and oil were aspirated off without disturbing the particles. All leftover particles, acetic acid, and oil were transferred to a new 5 mL tube and spun at 100 g for 2 minutes. The supernatant, which is primarily oil, was removed before adding 20% PFO in HFE oil (detangler) and vortexing on and off for 30 seconds to resuspend. The particles were then spun for 5 minutes at 100g, and the detangler was removed. This step was then repeated. The particles were transferred to a new tube, in which 2 mLs of PBS were added, and spun at 500g for 5 minutes. Ten percent Isopropanol was added, and the particles were spun at 3000g for 5 minutes. The particles were then resuspended in 3-4 mLs of PBS with calcium and magnesium.

2.5 Microparticle Droplet Generation: Dropwise Emulsion Method

A 3 mL syringe was filled with alginate, and another 3 mL syringe was filled with 0.5% acetic acid. A stir bar was added to a 30 mL beaker containing 8.2 mL of mineral oil and 300 uL of Span-80 (surfactant). The stir plate was turned on and set to 1200 rpm. The syringe containing acetic acid was pushed until one drop comes out, and the syringe containing alginate was pushed until the alginate reaches the Y-junction. Both syringes were attached to their own syringe pumps. The pump holding the alginate was set to 2.1 mL/min, while the pump with the acetic acid was set to 0.15 mL/min. The alginate pump was started immediately after the acetic acid pump. After the alginate was completely out, the acetic acid pump was stopped. The contents spun for 15 minutes, then 4% glacial acetic acid was added to the beaker and continue spinning for 1 hour.

2.6 Solvent Transfer/Particle Washing: Dropwise Emulsion Method

Following the 1-hour spin step, the contents of the 30 mL beaker were poured into a 15 mL conical tube. The tube were spun for 2 minutes at 500 g. All spin steps were performed at room temperature. The supernatant, which is mostly oil, was removed. Two mLs of detangler (50:50 octanol-1:mineral oil) were added to the pellet, which was vortexed on and off for 30 seconds to mix. It was then spun at 500 g for 3 minutes. The supernatant is removed, and the detangler step was repeated. After removing the supernatant again, 2 mLs of PBS were added to the pellet, which was vortexed to resuspend. It was spun at 500 g for 5 minutes. Two mLs of 100% isopropanol were added, and the tube was vortexed again to resuspend the particles. After spinning at 800g for 5 minutes, the particles were resuspended in 6-8 mLs of DPBS with calcium and magnesium and stored at 4°C.

2.7 Microparticle Stability

The particles were removed from the fridge and vortexed in the 15 mL tube for 30 seconds. They were then diluted using a 1:15 solution (280 µL DPBS and 20 µL particles). 10 uL of the diluted solution was placed in an imaging chamber and imaged via epifluorescent microscopy under 20x magnification. 20 µL of DPBS was added to the 15 mL tube containing the particles, then placed back in the fridge.

2.8 Particle Quantification (ImageJ)

Several ROIs were taken from the EPI images. The images were opened in ImageJ and converted to 8-bit. Based on the image, the scale was set using Analyze → Set Scale. Them, Process → Enhance Contrast was used to normalize the image and set saturated pixels to 0.35%. Process → Subtract Background was used to, select light background and set the radius to 50.0 pixels. The image threshold was adjusted using Yen or Otsu and set the threshold to 1-255. Process → Binary was used to fill holes, and Process → Open removed some of the background noise. Finally, Analyze Particles was used to obtain size data.

2.9 Drug Loading

A 10 mg/mL stock solution of Doxorubicin was made using 0.9% saline as the solvent. After performing solvent transfer, the stock solution was diluted down with 0.9% saline to 0.75-1 mg/mL for a total volume of 3 mL. The diluted solution was then put on the particles and mixed thoroughly. The particles were covered in tinfoil to protect them from light and placed on the rocker for 30 minutes at room temperature. They were then washed twice using a saline solution.

2.10 Loading Quantification

Both loaded and unloaded microparticles were placed with a known volume of 500 mM sodium citrate solution for 30 minutes to dissolve. A standard curve, preferably from the original DOX stock solution, was made by measuring the absorbance of various concentrations of the DOX stock solution (Figure 4). 100 uL of each solution was added to three wells in a 96-well clear-bottom black side plate. Once the microparticles have dissolved, the particle + sodium citrate solution were mixed and 100 uL of each solution was added to three separate wells. The absorbance was measured on the plate reader at 480 nm.

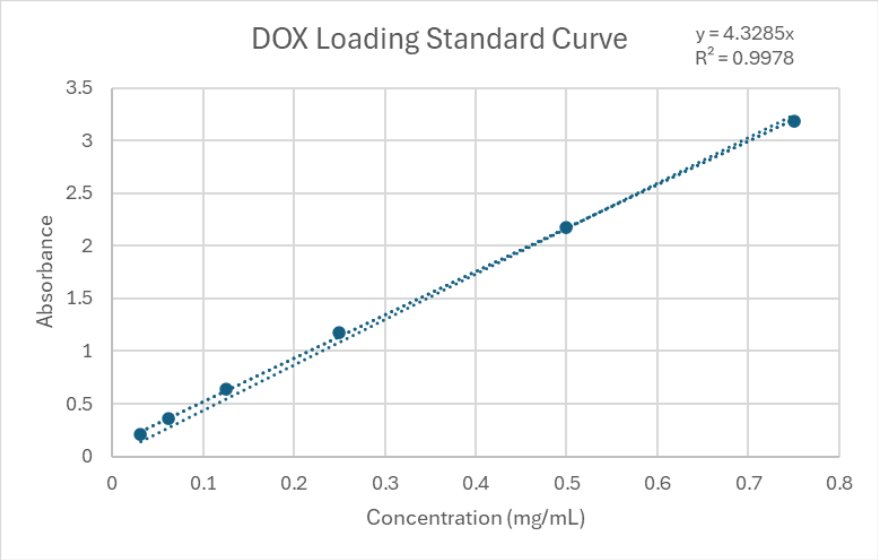

Figure 4. DOX standard curve for determining DOX-loading in microparticles. y = 4.3285x. with the y-intercept forced through 0,0. The high R^2 of 0.9978 indicates a strong linear relationship.

To create the standard curve, the average absorbance of each concentration of the dox stock solution was obtained and the concentration versus absorbance was plotted. From there, a line of best fit was obtained. The average absorbance of the

unloaded samples was subtracted from the average absorbance of the loaded samples. The line of best fit was used to determine the concentration of DOX in the particles from the absorbance. The concentration of DOX obtained from the standard curve was multiplied by the dilution ratio of particles to sodium citrate. Then, the added volume of DOX solution was multiplied by the concentration of DOX to obtain the total mass of drug in the particles. The total volume was divided by the volume of particles + the volume of the drug solution to obtain the true loading concentration. To determine the loading efficiency, the mass determined from the standard curve and dilution ratio was divided by the total mass of drug in the particles.

2.11 DOX Efficacy (Free Drug)

To confirm that DOX effectively causes 4T1 cell death and determine an optimal DOX killing concentration, wells with 4T1 cells were spiked with DOX at concentrations of 0.25 mg/mL, 0.35 mg/mL, 0.5 mg/mL, and 1 mg/mL. Controls consisted of a media only control and a media + saline control. After 48 hours, an alamar blue assay was performed to asses cell viability.

2.12 DOX Efficacy (Free versus Loaded)

To test if the drug payload remained functional post-encapsulation and release, alginate MPs were loaded with Doxorubicin (DOX) via incubation for 2 hours at room temperature. The DOX-loaded MPs were then incubated in PBS at room temperature for 3 hours. The DOX-laden PBS supernatant was collected and used to spike the 4T1 cell media at a concentration of 0.0985 mg/mL. Controls consisted of treatments with RPMI 1640 media, RPMI 1640 media plus saline, and RPMI 1640 media plus 0.0985

mg/mL free DOX. At 36 hours, an alamar blue assay was performed to determine cell viability.

2.13 DOX Efficacy Post Encapsulation (Varied Crosslinking)

A 24-well TC plate was seeded with 50,000 cells/well with 0.5 mL of RPMI1640 media per well. The plate was incubated for 48 hours until the cells were about ~80% confluent. The cells were washed with 1X PBS, and 400 uL of fresh media was added to each well. One hundred uL of 0.9% NaCl was added to three control wells. One hundred uL of unloaded 2% acetic acid particles were added to 3 wells, 100 uL of loaded 2% acetic acid particles were added to 3 wells, and 50 uL of loaded 2% acetic acid particles were added to 3 wells. The same was done for 6% acetic acid microparticles. The plate was placed on a rocker in the incubator for 48 hours.

2.14 Alamar Blue Assay

At the 48h time point, each well was washed with 1X PBS twice and 1mL of 1X alamar blue solution was added. The plate was placed in the incubator for 4 hours. The fluorescence was read using the plate reader at Excitation/Emission of 560/590 nm. Baseline viability was based on the media + saline control, with higher fluorescence corresponding to higher cell activity.

2.15 Statistical Analysis

All statistical analysis was performed using JMP Statistical Software. A one-way ANOVA and Tukey HSD were used to compare means for size data, DOX efficacy, and loading data. All bar graphs were made using MatLab.

Chapter 3

Results

3.1 Aim 1

3.1.1 Droplet Generation

To develop a protocol for generating monodispersed alginate droplets with efficient solvent transfer, two fabrication approaches were evaluated: dropwise emulsion and flow-focusing microfluidics (Figure 5). The dropwise emulsion method relies on mixing to disperse alginate into an immiscible phase, whereas the flow-focusing device generates droplets through controlled shearing at a microfluidic junction. The dropwise emulsion method enables rapid generation of alginate droplets, particularly when compared to the flow-focusing chip.

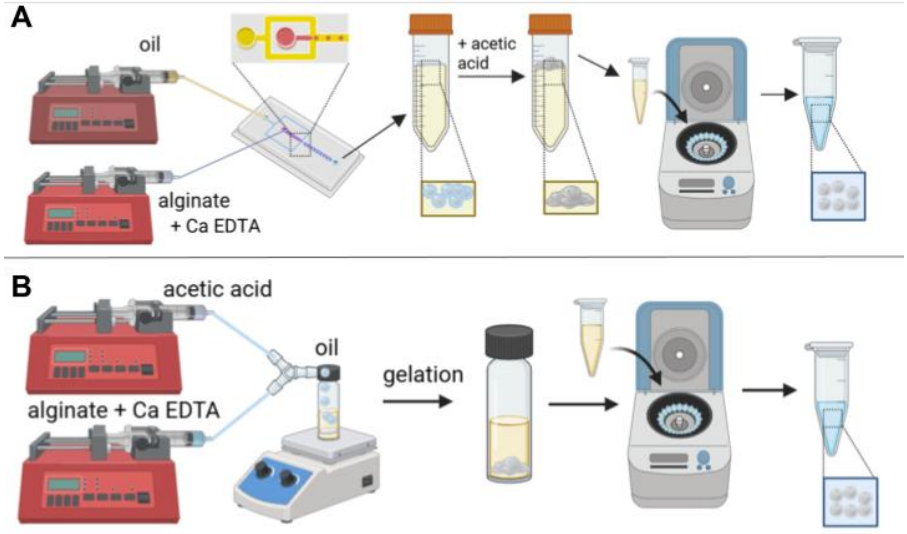

Figure 5. Schematic of droplet generation protocol for (A) microfluidic flow focusing chip and (B) dropwise emulsion methods.

Initial characterization focused on droplet morphology and production rate for each method. The flow-focusing chip method produced spherical alginate droplets that were highly uniform droplets with consistent morphology. On the other hand, those produced with the emulsion method were round but exhibited some defects, with variability in droplet size and morphology (Figure 6). The flow-focusing approach achieves better control over droplet size and uniformity, but it has a much lower throughput.

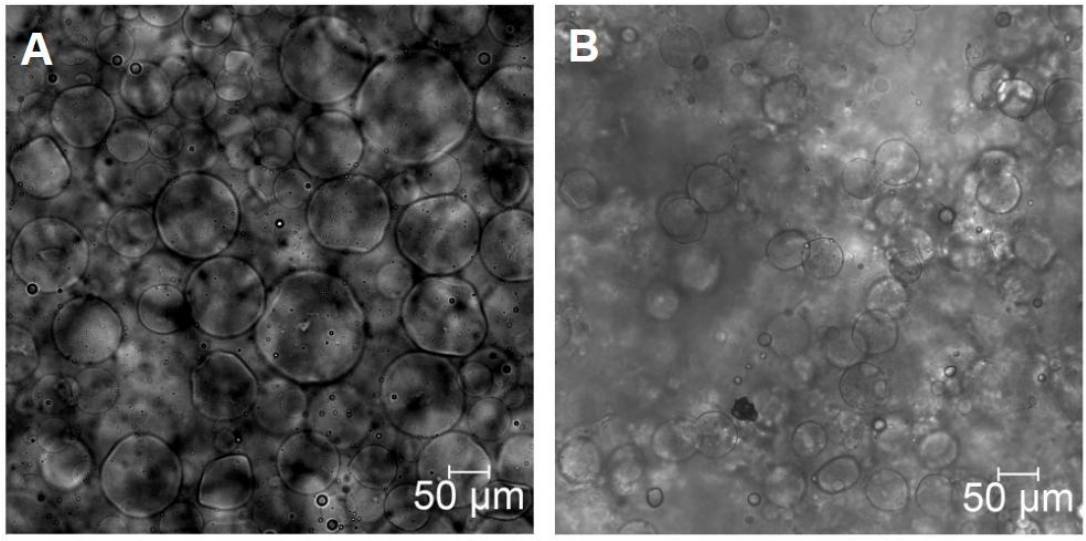

Figure 6. Alginate microparticles generated using the (A) dropwise emulsion method at 700 rpm and (B) flow focusing microfluidic chip (20x magnification).

3.1.2 Droplet Size Quantification between Batches

After particle generation, the particle sizes between batches were quantified and compared. Particles produced using the dropwise emulsion method at 700 rpm had an average size of 65.61 µm ± 22.08 µm, 66.19 µm ± 33.10 µm, and 79.9 µm ± 49.35 µm in batches 1, 2, and 3, respectively (Figure 7.A). A one-way ANOVA was performed on the data, indicating no significant difference in average particle size

among the groups (p = 0.385). Particles produced using the dropwise emulsion method at 1200 rpm had an average size of 57.05 µm ± 19.60 µm, 51.19 µm ± 19.20 µm, and 44.05 µm ± 25.05 µm in batches 1, 2, and 3, respectively (Figure 7.B). A one-way ANOVA was performed, indicating no significant difference in average particle size among the groups (p = 0.0687).

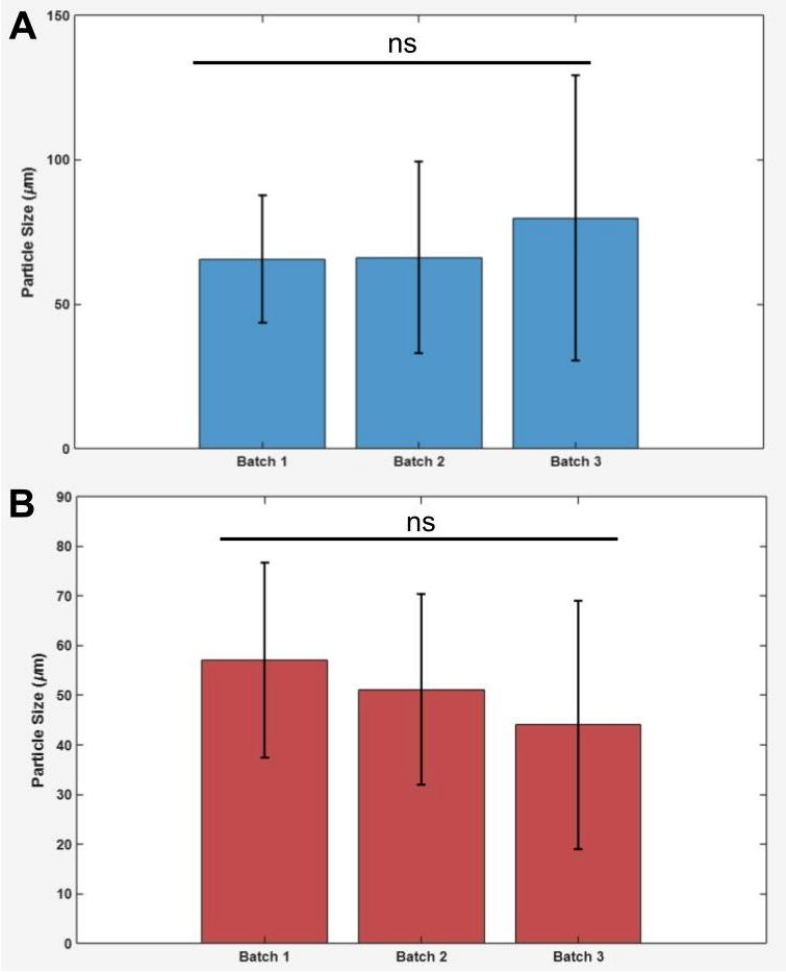

Figure 7. Average microparticle size among batches for those made at (A) 700 rpm: 65.61 µm ± 22.08 µm, 66.19 µm ± 33.10 µm, and 79.9 µm ± 49.35 µm in batches 1, 2, and 3, respectively, and (B) 1200 rpm: 57.05 µm ± 19.60 µm, 51.19 µm ± 19.20 µm, and 44.05 µm ± 25.05 µm in batches 1, 2, and 3, respectively (ns = no significance, n =3).

3.1.3 Droplet Size Quantification between Groups

After particle generation, the sizes between groups were quantified and compared. Particles produced using the flow-focusing chip had an average size of 47.36 µm ± 5.36 µm, while particles made using the dropwise emulsion method had an average size of 69.83 µm ± 34.83 µm and 53.3 µm ± 24.4 µm at 700 and 1200 rpm, respectively (Figure 8). Running a one-way on this data indicated there is a significant difference in particle sizes. A Tukey HSD was then performed, which showed significance between the 700 rpm group and the flow-focusing chip group ($p = 0.0175$), and between the 700 and 1200 rpm groups ($p = 0.0004$), but not between the 1200 rpm and flow-focusing chip groups. The flow-focusing device produced the smallest droplets overall and demonstrated the narrowest size distribution, indicating a high degree of monodispersity.

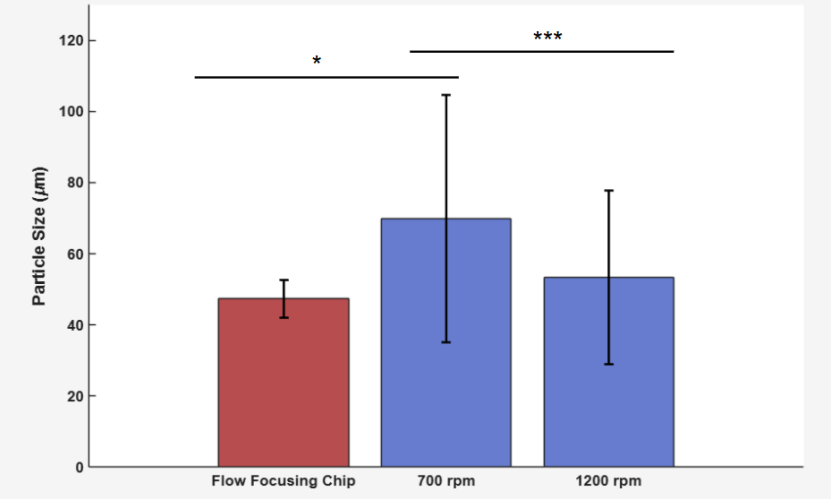

Figure 8. Average size of particles made using the dropwise emulsion method at 700 rpm (69.83 µm ± 34.83 µm) and at 1200 rpm (53.3 µm ± 24.4 µm), and the microfluidic chip (47.36 µm ± 5.36 µm,). (* $p < 0.05$, *** $p < 0.001$, $n = 3$).

3.1.4 Droplet Washing

Following droplet generation, a multi-step washing protocol was used to remove residual oil. After the initial centrifugation steps, phase separation was consistently observed. Removal of the supernatant effectively reduced the majority of the oil content, although residual oil remained with the pellet. To further improve oil removal, a detangling step using a 1:1 mixture of octanol-1 and mineral oil was introduced, and repeating this step further improved oil reduction (Table 1). No significant aggregation was observed post-washing, suggesting that the protocol effectively removed oil while preserving particle stability. This washing protocol enabled efficient solvent transfer from an oil-continuous phase to an aqueous environment, yielding clean, stable alginate particles suitable for downstream applications. Post washing, particle yield is on the order of a billion.

Table 1. A pass is defined as a clear microparticle pellet formed and separated from the oil phase in the centrifuge tube.

Condition	Outcome
One octanol wash	Fail
Two octanol washes	Pass
Two mL PBS on pellet	Pass
Final spin step @ 300 g	Fail
Final spin step @ 500 g	Pass

3.1.5 Droplet Storage Conditions

To determine optimal storage conditions, the particles were stored in DPBS with calcium and magnesium, and DPBS + calcium. After 72 hours, the particles were assessed via epifluorescent microscopy (Figure 9). The particles stored in DPBS with calcium and magnesium remained relatively stable, with minimal aggregation. Particles stored in DPBS + calcium showed a significant loss in integrity, along with a high degree of aggregation.

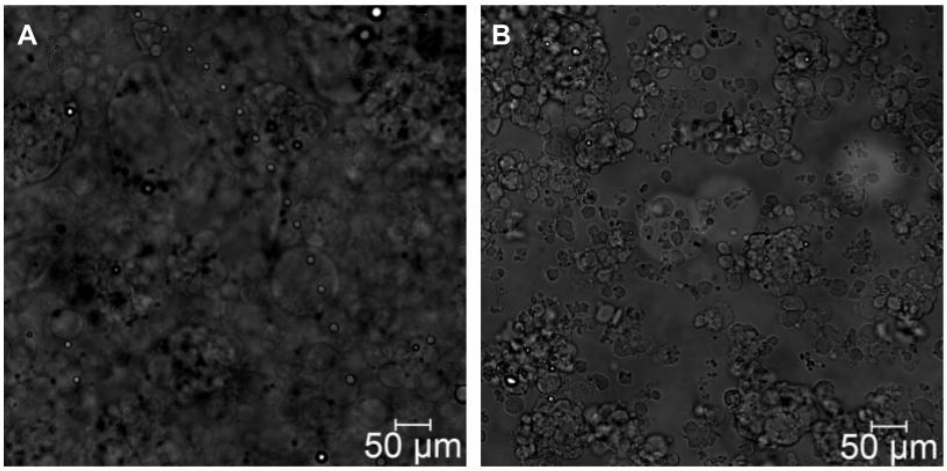

Figure 9. Alginate microparticles stored in (A) DPBS with calcium and magnesium and (B) DPBS + calcium after 72 hours at 4 °C (20X magnification).

3.1.6 Droplet Stability

The stability of alginate particles during storage was evaluated by measuring changes in average particle diameter over a 10-day period at 4 °C in DPBS supplemented with calcium and magnesium. The average sizes for particles on day 1 was 11.2 µm ± 4.7 µm, day 2 was 12.4 µm ± 3.5 µm, on day 3 was 9.9 µm ± 3.5 µm, on day 4 was 11.0 µm ± 3.6 µm, on day 6 was 11.6 µm ± 3.4 µm, and on day 10 was 10.5 µm ± 3.3 µm (Figure 10). A one-way ANOVA was performed on the average particle diameters for days 1-5 and day 10, and significance was found ($p = 0.0055$).

Following that, a Tukey HSD test was run, which found that there was a significant difference in particle size between days 2 and 3 ($p = 0.0017$), while all other groups showed no significant differences. Storing the particles at 4 °C and in a buffer that contains calcium and magnesium helps maintain particle stability and prevent premature degradation by maintaining alginate crosslinks. Since the particles are stable for 10 days in these storage conditions, they are suitable for downstream applications that require short-term storage.

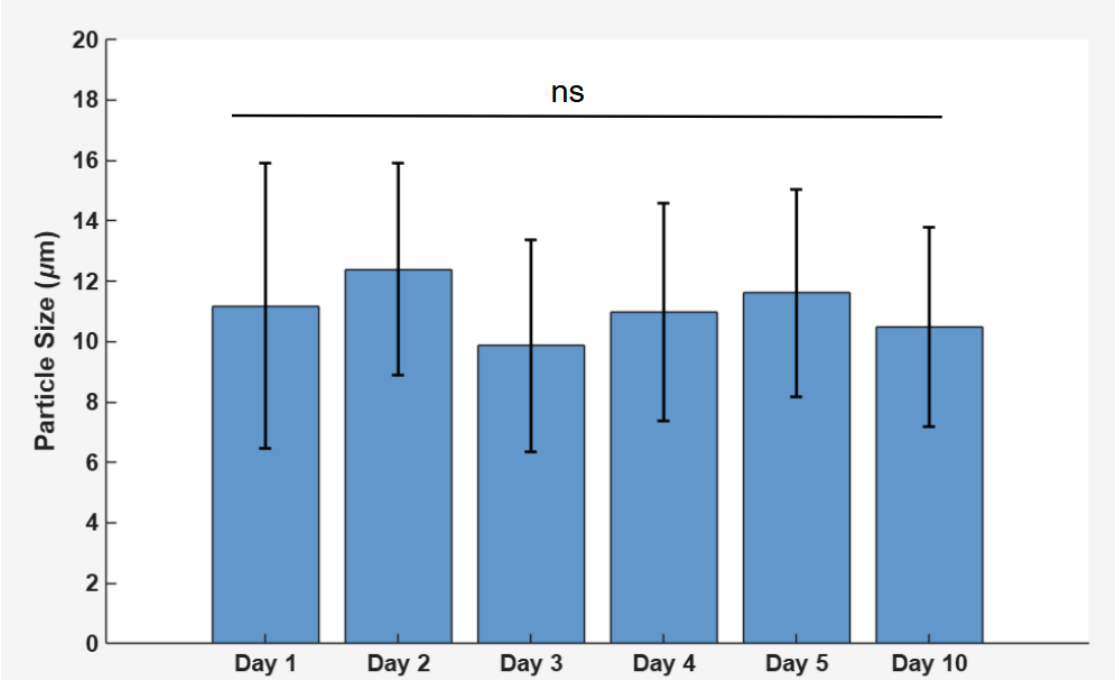

Figure 10. Microparticle diameter (μm) across days 1-5 and day 10 when stored in DPBS with calcium and magnesium at 4 °C. Day 1: 11.2 μm ± 4.7 μm, Day 2: 12.4 μm ± 3.5 μm, Day 3: 9.9 μm ± 3.5 μm, Day 4: 11.0 μm ± 3.6 μm, Day 6: 11.6 μm ± 3.4 μm, Day 10: 10.5 μm ± 3.3 μm (ns = not significant, n =3).

Across the 10-day storage period, the estimated total number of particles in the original 6.5 mL sample remained on the order of ~10^{13}, with values ranging from approximately 1.24 × 10^{13} to 2.03 × 10^{13} particles (Figure 11). The lowest particle number was observed on day 5 and the highest was seen on day 3. Intermediate values were observed on days 1 through 4, with no clear increasing or decreasing trend over time. The total particle concentration remained relatively stable throughout the storage period.

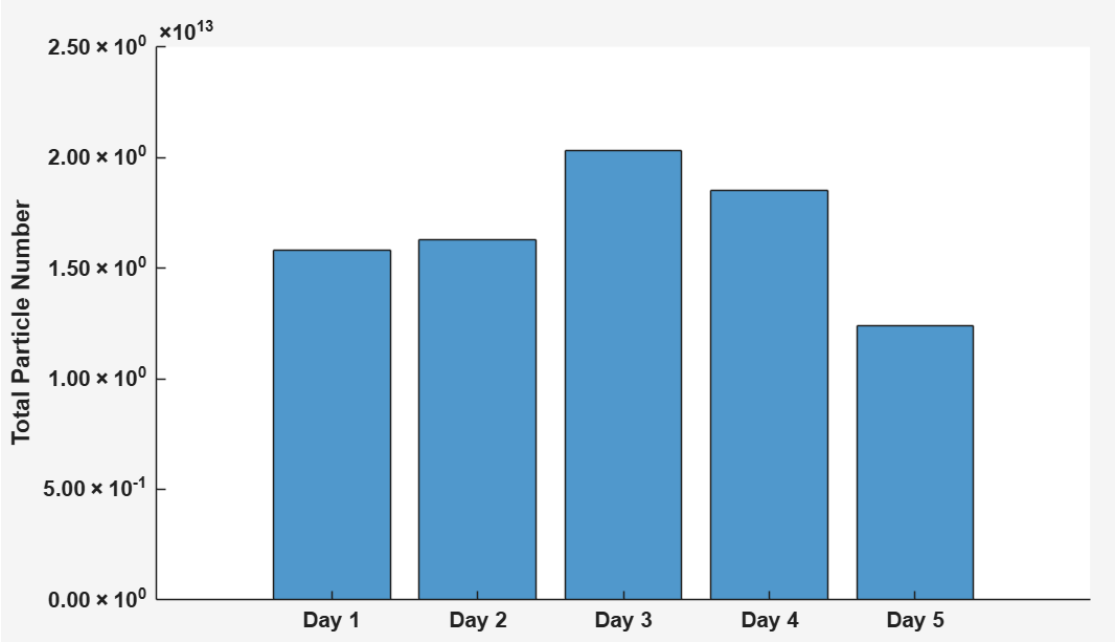

Figure 11. Total particle number in a 6.5 mL sample across days 1-5. Day 1: 1.58E13, Day 2: 1.63E13, Day 3: 2.03E13, Day 4: 1.85E13, Day 5: 1.24E13. (n =1).

3.2 Aim 2

3.2.1 Drug Mass and Loading Comparison

To evaluate loading across molecules of different sizes, particles were encapsulated with 500 kDa FITC-dextran and Doxorubicin (DOX). Both molecules were successfully encapsulated with comparable loading efficiencies (Table 2), with DOX showing a slightly higher efficiency of 15.76% compared to that of FITC-dextran, which had a loading of 14.82%. Despite this, the drug mass per particle differed substantially between the two groups. DOX-loaded particles contained a markedly higher mass per particle (0.213 μg) compared to FITC-dextran-loaded particles (0.013 μg). Particles with FITC-dextran were significantly larger (850,918 μm^3) than DOX encapsulated particles (246,949 μm^3). This data proves that molecules of varying molecular weights can be effectively encapsulated.

Table 2. Loading efficiency of Fluorescein-dextran and Doxorubicin loaded microparticles.

	Molecular Weight (kDa)	**Loading Efficiency**	**Drug Mass per Particle (μg)**	**Average Particle Volume (μm^3)**
FITC-Dextran	500	14.82%	0.013	850918
Doxorubicin (DOX)	0.543	15.76%	0.213	246949

3.2.2 Doxorubicin Loading

The morphology of DOX-loaded particles was assessed via epifluorescent microscopy. When DOX was encapsulated in particles made using the flow-focusing microfluidic chip, there was minimal particle aggregation (Figure 11.A). In contrast, when particles made using the dropwise emulsion method were encapsulated with DOX, significant clumping and particle aggregation occurred (Figure 11.B).

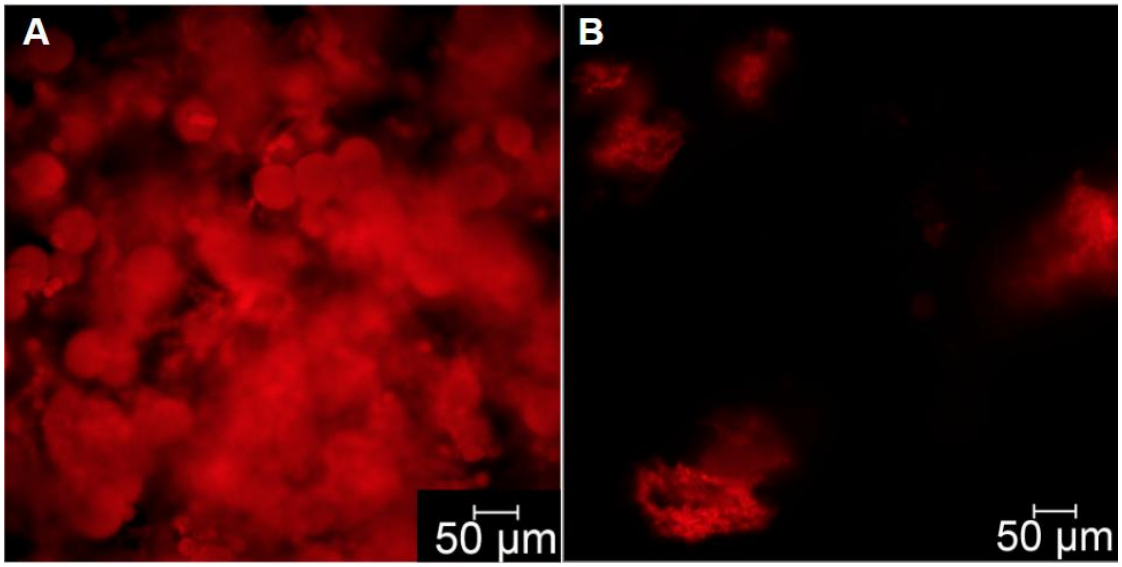

Figure 11. Doxorubicin-loaded microparticles made using the (A) flow focusing chip and (B) dropwise emulsion method (20x magnification).

When microparticles were loaded with 1 mg/mL DOX or higher, there was either complete aggregation or particle integrity was completely lost (Figure 12). When the loading concentration was reduced to 0.75 mg/mL for 30 minutes, less aggregation was observed. The concentration of DOX loaded and the diffusion time

were reduced beyond that; however, some degree of aggregation was still observed. Despite that, DOX was encapsulated in the particles.

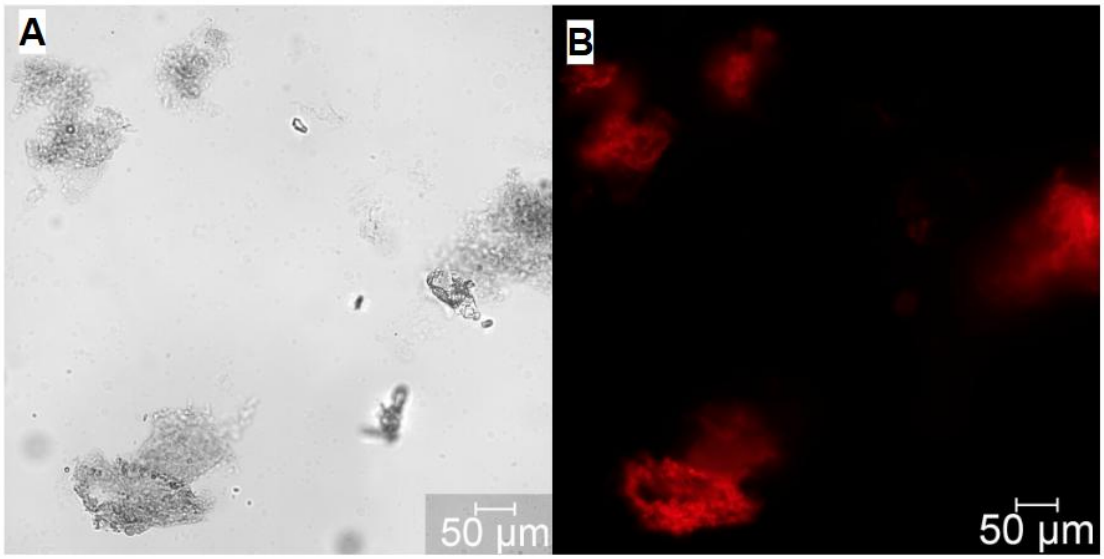

Figure 12. DOX loaded microparticles made using the dropwise emulsion method under (A) brightfield and (B) Cy5 far red channels, showcasing particle aggregation (20x magnification).

3.2.3 Crosslinking Density and Loading Efficiency

To assess whether crosslinking density affects loading efficiency, particles were crosslinked using either 2% or 6% acetic acid. In both groups, a total of 2.25 mg of DOX was introduced by incubating 1 mL of particles in 3 mL of drug solution. Following loading, the amount of DOX encapsulated within the particles was quantified for each condition. For particles crosslinked with 2% acetic acid, 1.0132 mg of DOX was successfully encapsulated, corresponding to a loading efficiency of 45.03% (Figure 13). For particles crosslinked with 6% acetic acid, 1.004 mg of DOX

was encapsulated, yielding a loading efficiency of 44.62%. The difference in encapsulated mass between the two conditions was 0.0092 mg, and the difference in loading efficiency was 0.41%. Overall, both crosslinking conditions produced similar levels of DOX encapsulation under identical loading conditions.

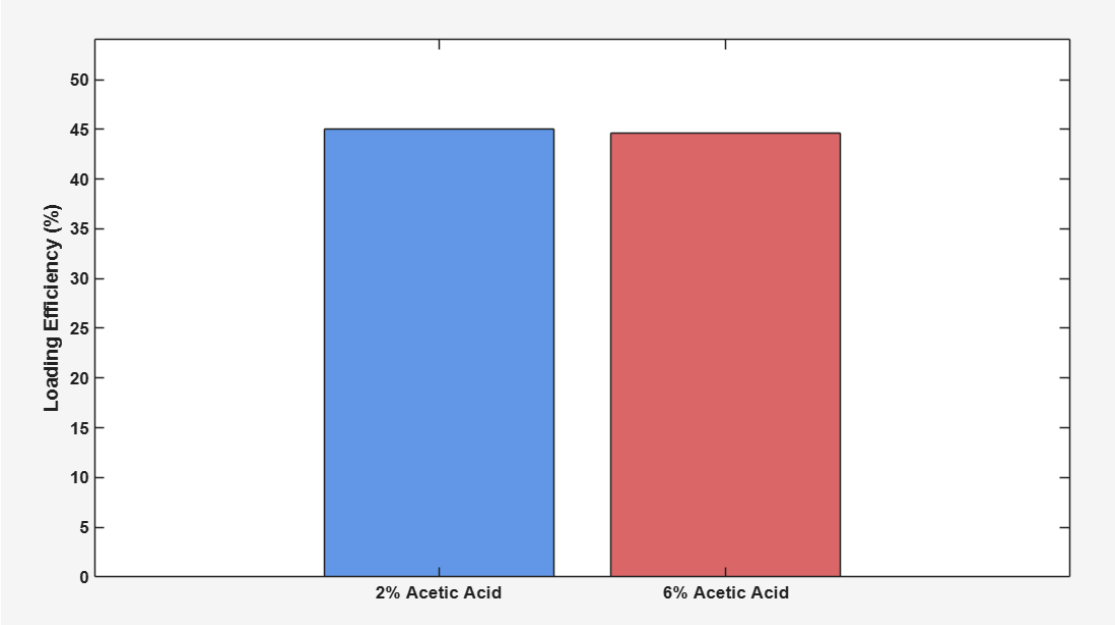

Figure 13. Loading efficiency of MPs made with 2% and 6% acetic acid (n = 1). The loading efficiency for MPs with 2% acetic acid is 45.03% and for 6% it is 44.62%.

3.2.4 Free DOX Efficacy on 4T1 Cells

To assess the efficacy of DOX on 4T1 cells, varying concentrations of free DOX were placed in wells with 4T1 cells for 48 hours. At t = 48 hours, the media-only control was used as a baseline for 100% cell viability. The media + saline group had an average viability of 88.4 ± 6.1%, the group treated with 0.25 mg/mL DOX had a viability of 20.8 ± 2.1%, the 0.35 mg/mL treatment group had a viability of 17.2 ± 4.1%, the 0.5 mg/mL treatment group had a viability of 10.9 ± 3.2%, and the 1 mg/mL

treatment group had a viability of 10.6 ± 1.7% (Figure 14). A one-way ANOVA was performed, which indicated significance ($p < 0.001$). A Tukey HSD was then performed, which showed significance between all groups except 0.25 mg/mL and 0.35 mg/mL ($p = 0.7162$), and 0.35, 0.5, and 1 mg/mL ($p > 0.1908$).

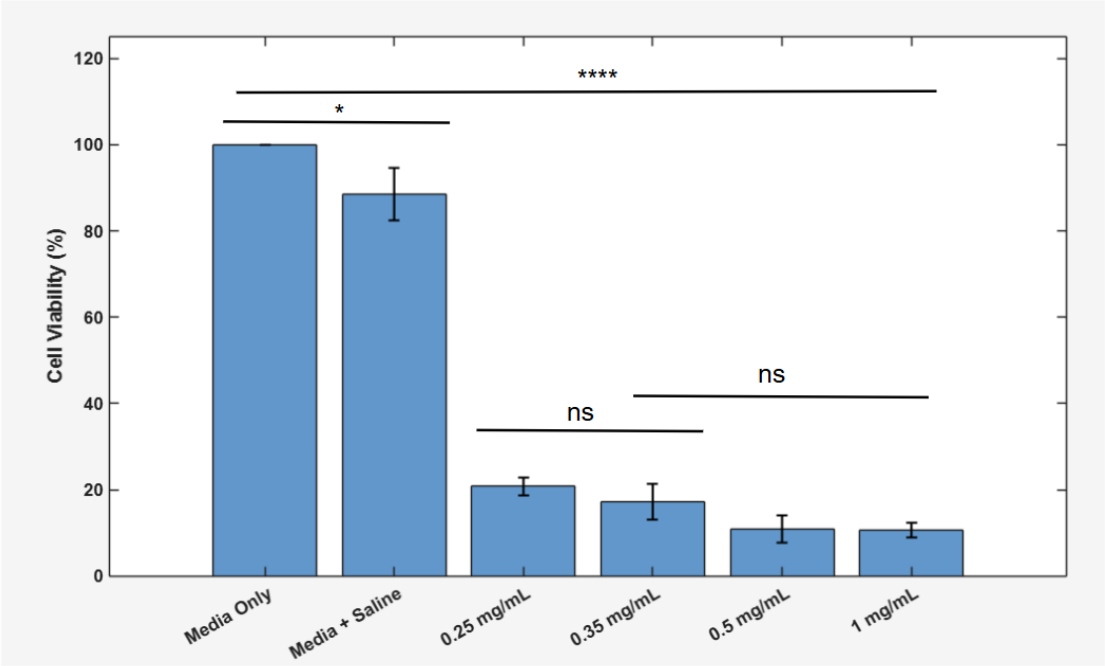

Figure 14. Cell viability of 4T1 cells after being exposed to 0.25, 0.35, 0.5, and 1 mg/mL of DOX for 48 hours. The media + saline group had an average viability of 88.4 ± 6.1%, the 0.25 mg/mL DOX treatment group had a viability of 20.8 ± 2.1%, the 0.35 mg/mL treatment group had a viability of 17.2 ± 4.1%, the 0.5 mg/mL treatment group had a viability of 10.9 ± 3.2%, and the 1 mg/mL treatment group had a viability of 10.6 ± 1.7%. The media only control was treated as 100% cell viability baseline (n = 3, ns = not significant, * $p < 0.05$, **** $p < 0.0001$).

3.2.5 DOX Efficacy Post-Encapsulation

To assess the efficacy of DOX post-encapsulation, particles were encapsulated with DOX. They were placed in 0.9% Saline for 6 hours to allow DOX release, and the DOX-laden saline was put on 4T1 cells. After 36 hours, the alamar blue assay

indicated that 4T1 cells treated with free DOX had a cell viability of 39.2%, while those treated with the microparticle-released DOX had a viability of 36.5% (Figure 15). The media-only control served as a baseline for 100% cell viability and metabolic activity, and the media + saline group had no decrease in cell viability compared to the media-only control.

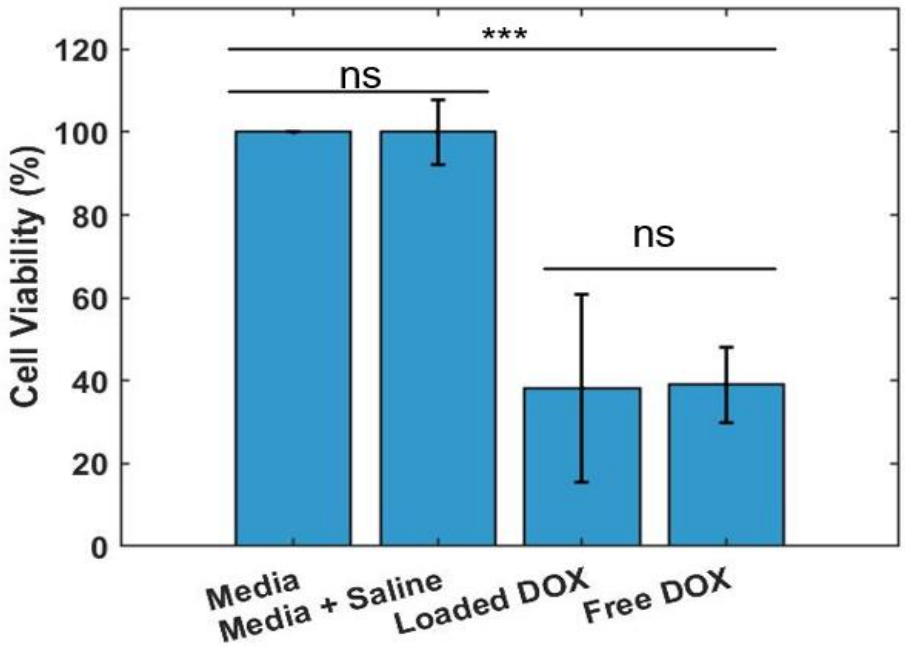

Figure 15. 4T1 cell viability after exposure to Doxorubicin (DOX) for 36 hours. The media only control served as a 100% viability baseline. 4T1 cells treated with free DOX had a cell viability of 39.2% ± 42.6%, and those treated with the released DOX had a viability of 36.5% ± 11.9%. The media + saline group also had a viability of 100% ± 7.7% (n=3; ns = not significant, *** $p < 0.001$).

3.2.6 DOX Treatment with Varying Crosslinking Densities

To assess whether crosslinking density impacts DOX release, particles crosslinked with both 2% and 6% acetic acid were loaded with 0.75 mg/mL DOX and placed with 4T1 cells. At t = 48 hours, cell viability was measured using alamar blue.

The 6% unloaded group showed a viability of 136 ± 11.7%, while the 6% loaded 50 µL and 100 µL groups showed viabilities of 39.2 ± 1.31% and 39.7 ± 1.87%, respectively (Figure 16). The 2% unloaded (100 µL) group had a viability of 128 ± 16.7%, while the 2% loaded 50 µL and 100 µL groups showed viabilities of 39.9 ± 1.53% and 37.2 ± 1.15%, respectively. Free doxorubicin at 2% concentration resulted in a viability of 40.3 ± 1.23%, and free doxorubicin at 6% concentration resulted in a viability of 38.8 ± 0.069%. A one-way ANOVA was performed, which indicated significance ($p < 0.0001$). A Tukey HSD test was then run, which indicated no significance between the 2% unloaded and 6% unloaded; however, those two groups were significantly different than all DOX conditions ($p < 0.0001$) and the media control ($p = 0.0002$ and $p = 0.0032$ for 6% unloaded and 2% unloaded, respectively). The media control group was significantly different than all DOX conditions, too ($p < 0.0001$).

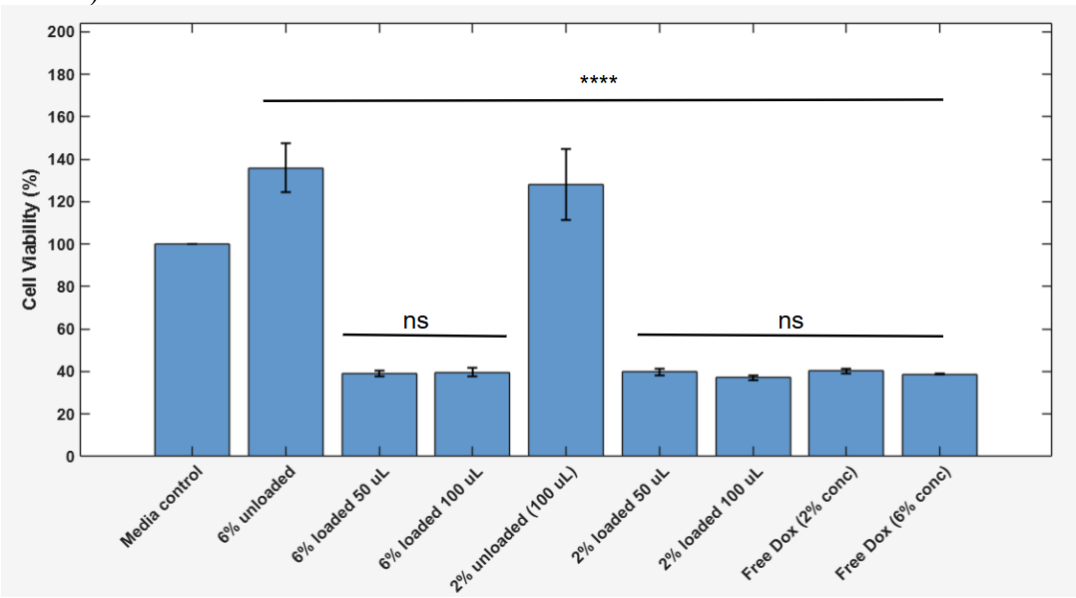

Figure 16. 4T1 cell viability after exposure to Doxorubicin (DOX) for 48 hours. The media only control served as a 100% viability baseline. The 6% unloaded group had a 136 ± 11.7% viability, the 6% loaded 50 µL and 100 µL groups had viabilities of 39.2 ± 1.31% and 39.7 ± 1.87%, respectively. The 2% unloaded group had a viability of 128 ± 16.7%, while the 2% loaded 50 µL and 100 µL groups had viabilities of 39.9 ± 1.53% and 37.2 ± 1.15%, respectively. Free doxorubicin at 2% concentration resulted in a viability of 40.3 ± 1.23%, and free doxorubicin at 6% concentration resulted in a viability of 38.8 ± 0.069%. (n=3; ns = not significant, **** $p < 0.0001$).

Chapter 4

Discussion

4.1 Aim 1: Develop an alginate droplet generating protocol for monodispersed droplets and efficient solvent transfer

In Aim 1, the alginate microparticles were characterized in order to develop and optimize a robust microfluidic protocol for generating monodispersed droplets with efficient solvent transfer while maintaining particle stability in storage. Overall, particle production and integrity were verified via microscopy, which also showcased the efficacy of the solvent transfer. Size and quantification data indicate a tradeoff between droplet uniformity and production rate depending on the fabrication method, while also demonstrating that the washing and storage conditions play a major role in maintaining particle quality.

In terms of particle size and morphology, those made using the flow-focusing microfluidic chip consistently produced the most uniform-sized, spherical particles. On the other hand, the dropwise emulsion method produced particles that were more variable in both size and morphology. This is likely due to less-controlled mixing conditions, since droplet breakup is influenced more by bulk fluid motion [52]. While the dropwise emulsion method enables rapid generation of alginate droplets, it yields greater size variability even at higher mixing speeds. Conversely, the flow-focusing approach achieves superior control over droplet size and uniformity but at the cost of reduced throughput. Other studies performed have also found this to be true [53]. This tradeoff between droplet uniformity and throughput is consistent with prior work in microfluidic alginate biomaterials, where lithographically defined PDMS-templated

channels yield highly monodisperse features at the cost of throughput compared with bulk emulsion approaches [40 , 51]. These findings helped inform the selection of droplet-generation conditions for subsequent experiments that required high yield and more efficient material use.

When using the dropwise emulsion generation method, increasing the mixing speed from 700 rpm to 1200 rpm decreased both particle size and variability. This suggests that higher shear forces in the emulsion system can partially compensate for the decreased control and precision, bringing particle size closer to what was achieved with the microfluidic flow-focusing chip. Additionally, there is minimal variability in size differences between batches generated under the same conditions, indicating that the protocol developed is both reliable and repeatable.

Over the 10-day storage period at 4 °C, particle size remained consistent, as no statistical significance was found. This indicates that storing particles in DPBS supplemented with calcium and magnesium is sufficient to maintain particle integrity. Although calcium is responsible for alginate crosslinking, these results suggest that magnesium also plays a role in stabilizing the system, likely by maintaining ionic balance and strengthening the polymer network [54]. More broadly, the mechanical, transport, and stability properties of alginate hydrogels are highly tunable through manipulation of crosslinking chemistry and divalent cation environment, and similar layered or composite alginate constructs maintain integrity under multi-week culture when crosslink chemistry is preserved [45, 46]. The slight fluctuations in microparticle size seen across days can be attributed to measurement variability, as no significant differences in size. This is supported by the fact that particle concentration stayed on the order of 10^{13} particles throughout days 1-5. The ability for the particles to be stored

over an extended period is helpful when designing or executing experiments that run over the course of several days.

This aim helps establish a functional and repeatable workflow for alginate particle fabrication, washing, and storage. The dropwise emulsion method is better suited for high-throughput production, especially at higher mixing speeds, and can be used to produce particles of varying sizes, when compared to the microfluidic flow focusing chip. The washing protocol effectively removes oil without causing aggregation, and particles can be stored in DPBS supplemented with calcium and magnesium without losing integrity. The ability to generate particles entirely in the aqueous phase with tunable sizes makes this generation system a promising platform for developing delivery vehicles tailored to a range of applications.

4.2 Aim 2: Determine payload functionality and release from the MPs along with how a material change will impact release

In Aim 2, the loading and release of molecules from the alginate microparticles were characterized to examine whether they could effectively encapsulate molecules of differing sizes and determine if changes in crosslinking density impact these parameters. Along with that, it helped ensure drug efficacy post-encapsulation. All of these are important for engineering a delivery vehicle with tunable loading and release parameters. Initial experiments loading with DOX and FITC-Dextran verified that molecules of varying sizes can be effectively encapsulated, and further testing showcased that loaded molecules remained effective post-encapsulation.

When comparing the loading of 500 kDa FITC-dextran and Doxorubicin (DOX), both were successfully incorporated into the particles, with encapsulation

efficiencies of 14.82% and 15.76%, respectively. FITC-Dextran and DOX were used in this system because their molecular weight differs greatly, with FITC-Dextran being 1000x larger than DOX. The similarity in encapsulation efficiencies suggests that within the tested range, molecular size alone does not limit encapsulation efficiency in this system; however, the large difference in drug mass per particle indicates that particle size and volume play a greater role in determining total payload capacity than loading efficiency alone. Specifically, FITC-dextran–loaded particles exhibited significantly larger volumes than DOX-loaded particles, which may have contributed to differences in absolute drug mass per particle despite similar percentage loading.

Further analysis of DOX-loaded MP morphology highlighted differences in particle integrity post-loading. Particles produced via the flow-focusing microfluidic chip maintained structural integrity with minimal aggregation during DOX encapsulation, whereas those generated using the dropwise emulsion method exhibited severe clumping and aggregation. This suggests that microfluidic chip fabrication yields more mechanically and chemically stable particles, likely due to more controlled crosslinking architecture [55]. The differences in integrity became more pronounced at higher DOX concentrations, as dropwise emulsion particle integrity was compromised entirely at concentrations ≥1 mg/mL. Reducing the loading concentration and diffusion time mitigated aggregation, though it did not eliminate it. These findings indicate that DOX loading is sensitive to both concentration and loading time, due to its small molecular size and high diffusivity, which may interfere with particle–particle interactions or crosslink stability at higher concentrations. Other studies with DOX and alginate have indicated that while DOX does not necessarily

ruin the integrity of particles, it can promote more rapid swelling or degradation [56]. While the dropwise emulsion method can achieve DOX encapsulation, it may require further optimization to prevent aggregation and improve particle uniformity.

Crosslinking density's impact on drug loading was also assessed, comparing particles prepared using either 2% or 6% acetic acid. Both conditions produced nearly identical loading efficiencies of ~45%, with only a 0.41% difference between groups. This minimal variation suggests that crosslinking density does not significantly impact DOX uptake under identical loading conditions. Photocrosslinked alginate systems with stiffness varied by nearly an order of magnitude (approximately 3 to 12 kPa) similarly demonstrate that broad changes in network density are required to meaningfully alter solute interaction with the gel matrix [45]. However, the obtained result varies from those found in previous studies, where it has been found that drug loading, encapsulation, and release are significantly impacted by crosslinking density [57]. Increased crosslinking density creates a more dense polymer network that typically leads to a lower loading capacity. This could be a result of only altering the acetic acid concentration by 4%. Additionally, while efficiency remained unchanged, crosslinking may still play a role in mechanical stability or release kinetics, which were not directly assessed here. The similarity in loading behavior also suggests that DOX diffusion into the particles is not significantly affected by moderate changes in crosslinking density.

Based on previous literature, Doxorubicin has been shown to effectively kill 4T1 and other cancer cell lines *in vitro* [58]. To confirm this, free DOX of varying concentrations (0.25, 0.35, 0.5, 1 mg/mL) was placed on 4T1 cells. At t = 48 hours, free DOX demonstrated a clear dose-dependent reduction in cell viability,

decreasing from 20.8 ± 2.1% at 0.25 mg/mL to 10.9% and 10.6% at concentrations of 0.5 mg/mL and 1 mg/mL, respectively. The lack of statistical significance between the higher concentration groups suggests that maximal cytotoxicity is reached at relatively low DOX concentrations in this system, consistent with the high potency of DOX. Importantly, the saline-treated control group maintained high viability of 88.4%, confirming that observed cytotoxicity was a result of the DOX, rather than of the media or saline solution the cells were sitting in.

Along with that, DOX remains functional post loading and release. Cells treated with DOX released from particles exhibited 38.2% viability compared to 39% viability in the free DOX condition, indicating that the encapsulation and release process does not significantly diminish drug efficacy. This suggests that DOX retains bioactivity following diffusion through the particle matrix and into the surrounding environment. The similarity between these conditions also demonstrates that encapsulation does not chemically inactivate the drug nor substantially delay its therapeutic action within the tested timeframe.

When evaluating the impact of crosslinking density on drug release, both 2% and 6% acetic acid–crosslinked particles produced comparable effects. Viability in DOX-loaded groups was consistently reduced to ~37–40% across all conditions, regardless of crosslinking density or particle volume. In contrast, unloaded particle controls exhibited significantly higher viabilities (128–136%), which were statistically distinct from all DOX-treated groups. This elevated viability in unloaded conditions is a result of increased metabolic activity in cells because of particle presence. Although previous studies indicate that alginate is typically biologically inert, there are likely metabolic stimulation artifacts associated with particle exposure rather than true

proliferative increases, particularly since media controls remained stable at baseline [59]. Since there are no significant differences between 2% and 6% unloaded groups, this suggests that crosslinking density does not meaningfully influence baseline cytocompatibility or metabolic response in the absence of drug loading. This indicates that neither crosslinking density nor particle loading volume substantially alters the functional delivery of DOX once released. Collectively, these findings demonstrate that the microparticle system can maintain DOX bioactivity post-encapsulation while producing consistent cytotoxic outcomes comparable to free drug exposure. This versatility positions the platform alongside the broader class of engineered carriers, including liposomes, polymeric nanoparticles, and lipid nanoparticles, that have been deployed across oncology, infectious disease, and maternal-fetal medicine, but with the added advantage of microparticle-scale residence in lymphoid tissue [1, 35].

This aim helped establish that the system provides an effective and versatile platform for drug delivery. It enables encapsulation of both small and large molecules, maintains drug efficacy after release, and produces consistent biological outcomes independent of moderate variations in fabrication or crosslinking conditions.

Overall, this study demonstrates that a reliable alginate microparticle droplet generation system has been established that yields particles completely in the aqueous phase. The MPs can effectively encapsulate small-molecule drugs, allowing them to deliver a functional payload to cancer cells. This microparticle system also offers flexibility, as this study has shown that multiple different sizes of molecules can be loaded into the particles. Altogether, these results indicate that the microparticles are an effective delivery vehicle with tunable encapsulation and release parameters that can be leveraged for sustained release of a drug. This can enhance the amount of drug

delivered to the site of metastasis in the lymph node while reducing off-target accumulation, thereby creating an improved delivery vehicle.

Chapter 5

Limitations, Future Directions, & Conclusions

This study demonstrated that alginate microparticles have the potential to act as an effective delivery vehicle, offering tunable loading and size parameters. The dropwise emulsion microparticle system is a robust and adaptable platform for drug encapsulation and delivery. The system successfully encapsulated both small molecules (DOX) and large macromolecules (500 kDa FITC-dextran) with comparable loading efficiencies, indicating broad applicability across molecular sizes. However, several limitations should be considered. First, the presence of particle aggregation at higher DOX loading concentrations suggests that there are constraints on the maximum drug loading capacity without compromising particle integrity. This may restrict the system's applicability for high-dose delivery unless there is further optimization, and it prevented DOX release studies from being performed. Future studies should further investigate what the ideal DOX loading conditions are to mitigate or prevent particle aggregation. Finally, while crosslinking density was varied, the range tested (2% vs. 6% acetic acid) may have been too narrow to produce meaningful differences in loading or release behavior. Broader parameter variation may be necessary to fully understand how crosslinking influences particle performance. Surface engineering strategies developed for nanoparticle systems, including PEGylation, peptide coating, and rational protein corona modulation, may also be adaptable to mitigate aggregation and improve colloidal stability of drug-loaded alginate microparticles at higher payload concentrations [26].

While DOX is a well-established chemotherapeutic, it has also been shown to be toxic to non-cancerous cells [60]. Future directions could include loading the

particles with STING agonist or another immunologically relevant molecule. STING agonists, which are molecules that mimic or enhance the action of natural ligands that bind to STING receptors, are engineered as an immunotherapy to immune cells [61]. Targeted delivery of immunomodulatory cargo to the lymph node specifically has been highlighted as a critical unmet need across the physiological barrier drug delivery field, with very few clinical-stage carriers currently designed for LN-resident immune modulation [1]. Recent proof-of-concept work demonstrating LNP-mediated delivery of cytokine mRNAs to a tissue-resident cell population, producing local immunomodulation without systemic exposure, illustrates the feasibility of cell- or tissue-targeted immunoengineering payloads that could be adapted to a microparticle delivery format [34, 62]. STINGa causes the production of inflammatory cytokines, including type I interferons, which can help the immune system attack cancer cells by reprogramming the suppressive phenotype into a pro-inflammatory response. Type I interferons lead to an upregulation of co-stimulatory molecules, such as CD40 and CD80, and promote dendritic cell (DC) maturation. Mature DCs increase the expression of major histocompatibility complex (MHC) class I molecules, which are essential for presenting tumor-associated antigens to T cells. Therefore, STINGa helps enhance the antigen-presenting capabilities of DCs, allowing them to initiate antitumor immunity and drive robust antitumor responses.

Other future work should focus on characterizing long-term release kinetics to determine whether these microparticles can achieve sustained and controlled drug delivery. Extending release studies over several days or weeks, coupled with mathematical modeling, would provide deeper insight into diffusion mechanisms and matrix degradation. Along with that, other future work should include repeating the

loading efficiency and stability experiments to achieve n > 1 to further confirm the results obtained in this study.

Finally, the downstream goal is to wrap these MPs in Jurkat cell membranes, creating a T cell-mimetic membrane-wrapped microparticle (T3MP, Figure 3). The membrane wrapped component will help the MPs traffic to and target the lymph node, where the cargo can then be released, targeting the lymph node resident cancer cells. Importantly, all DOX efficacy-related findings should be validated in more physiologically relevant models, including 3D cell cultures and *in vivo* studies. Such models would allow assessment of particle distribution, drug release in complex environments, and potential improvements in therapeutic index compared to free drug delivery. All experiments were conducted *in vitro* using 4T1 cells, which, while a well-established breast cancer cell line, do not fully capture the complexity of the *in vivo* tumor microenvironment. Factors such as vascularization, immune interactions, and drug clearance are not represented, limiting direct translation of these results to clinical settings. Additionally, since temperature, pH, and protein content can all impact drug behavior, this is an important step to better understand how loaded particles will behave both in the bloodstream and in tumor microenvironments [63]. With that, the Jurkat membrane wrapping will alter drug release kinetics, which is important to understand before moving to *in vivo* work. Three-dimensionally accurate reconstructions of murine lymph nodes, capturing lobule and HEV geometry with expert-level fidelity, provide a digital-twin framework that can be coupled with these in vivo studies to predict spatial drug distribution and inform iterative design of T3MP delivery parameters [5, 64]. Microphysiological systems, including modular perfusion-ready organ-on-chip platforms, parallel-plate flow chambers with tunable substrate

mechanics, transwell-based barrier models with defined stromal compartments, and tissue-specific MPS devices that recapitulate microbial, immune, and pathogenic interactions, offer a controlled, physiologically relevant intermediate between bench and animal that should be leveraged to characterize microparticle release, uptake, and immune interactions across multiple tissue contexts before in vivo deployment [65-70]. Safety profiling for any LN-targeted carrier will additionally need to anticipate gestational, sex-, and disease-state-dependent effects on biodistribution and immune response, consistent with translational roadmaps recently proposed for nanoparticle therapeutics in vulnerable patient populations [71].

Beyond the experimental optimization above, computational protein design is becoming a powerful tool to engineer the protein and peptide components of next-generation T3MP systems. Protein language models have now been shown to predict protein-protein interactions across diverse organisms with high accuracy, capture cross-species taxonomic structure in their learned representations, and produce general-purpose semantic embeddings of biological sequences that can be reused for downstream design tasks [72,73,74]. Building on these representations, generative protein language models, including discrete diffusion approaches and architectures that incorporate explicit functional annotation vocabularies and improved bidirectional attention, open the door to designing custom targeting peptides, antibody fragments, or membrane-anchored ligands that could be displayed on the T3MP surface to enhance lymph-node-resident cell binding, antigen presentation, or controlled cargo release [75, 76, 77].

Microparticle fabrication method was shown to significantly impact morphology and stability, with flow-focusing microfluidics producing more uniform

and less aggregated particles compared to the dropwise emulsion method. For the purposes of this study, the dropwise emulsion generation system proved to be a more efficient generation method, with a higher throughput and tunable particle size. In terms of DOX loading, although higher drug loading concentrations led to aggregation, optimized conditions still enabled effective encapsulation. Importantly, DOX retained its cytotoxic efficacy following encapsulation and release, with the microparticle-released drug producing effects nearly identical to those of free DOX in 4T1 cells. Crosslinking density, within the tested range, did not significantly affect loading efficiency or cytotoxic outcomes, suggesting that the system is relatively robust to moderate fabrication variations. Overall, these results support the potential of this platform as an effective drug-delivery vehicle that maintains drug bioactivity while offering tunability in particle design. With further optimization and validation, this system shows promise for applications in targeted and controlled therapeutic delivery.

REFERENCES

[1] K. M. Nelson, M. J. Donzanti, O. S. Mhatre, and J. P. Gleghorn, "Advancing Drug Delivery Through Complex Physiological Barriers in the Brain, Lymph Node, and Placenta," *Annu Rev Biomed Eng*, vol. 28, no. 1, pp. 337–359, May 2026, doi: 10.1146/annurev-bioeng-102723-021307.

[2] I. Bujoreanu and V. Gupta, "Anatomy, Lymph Nodes," in *StatPearls*, Treasure Island (FL): StatPearls Publishing, 2026. Accessed: Apr. 26, 2026. [Online]. Available: http://www.ncbi.nlm.nih.gov/books/NBK557717/

[3] "Introduction to lymph nodes," Kenhub. Accessed: Apr. 26, 2026. [Online]. Available: https://www.kenhub.com/en/library/anatomy/lymph-nodes

[4] P. He, H. Tang, Y. Zheng, Y. Xiong, H. Cheng, J. Li, Y. Zhang, G. Liu, "Advances in nanomedicines for lymphatic imaging and therapy," *J Nanobiotechnology*, vol. 21, p. 292, Aug. 2023, doi: 10.1186/s12951-023-02022-x.

[5] M. A. Kibler, M. D. Miller, M. J. Donzanti, and J. P. Gleghorn, "Confocal-Compatible Workflow for Sectioning, Staining, and Imaging Serial Vibratome Sections for 3D Anatomical Reconstruction of the Lymph Node," *bioRxiv*, p. 2025.10.29.685350, Nov. 2025, doi: 10.1101/2025.10.29.685350.

[6] E. Boghaert, J. P. Gleghorn, K. Lee, N. Gjorevski, D. C. Radisky, and C. M. Nelson, "Host epithelial geometry regulates breast cancer cell invasiveness," *Proc Natl Acad Sci U S A*, vol. 109, no. 48, pp. 19632–19637, Nov. 2012, doi: 10.1073/pnas.1118872109.

[7] S. Karaman and M. Detmar, "Mechanisms of lymphatic metastasis," *J Clin Invest*, vol. 124, no. 3, pp. 922–928, Mar. 2014, doi: 10.1172/JCI71606.

[8] B. Hayward-Piatkovskyi, C. R. Gonyea, S. C. Pyle, K. Lingappan, and J. P. Gleghorn, “Sex-related external factors influence pulmonary vascular angiogenesis in a sex-dependent manner,” *Am J Physiol Heart Circ Physiol*, vol. 324, no. 1, pp. H26–H32, Jan. 2023, doi: 10.1152/ajpheart.00552.2022.

[9] B. Hayward-Piatkovskyi, C. N. Clark, C. R. Gonyea, K. Lingappan, J. P. Gleghorn, “Pro-angiogenic effects of dihydrotestosterone on angiogenesis in fetal pulmonary endothelial cells with implications for bronchopulmonary dysplasia.” *American Journal of Physiology, Lung Cellular and Molecular Physiology* (in revision). 2025.

[10] J. T. Morgan, J. Shirazi, E. M. Comber, C. Eschenburg, and J. P. Gleghorn, “Fabrication of centimeter-scale and geometrically arbitrary vascular networks using in vitro self-assembly,” *Biomaterials*, vol. 189, pp. 37–47, Jan. 2019, doi: 10.1016/j.biomaterials.2018.10.021.

[11] J. Shirazi, J. T. Morgan, E. M. Comber, and J. P. Gleghorn, “Generation and morphological quantification of large scale, three-dimensional, self-assembled vascular networks,” *MethodsX*, vol. 6, pp. 1907–1918, 2019, doi: 10.1016/j.mex.2019.08.006.

[12] H. Ji, C. Hu, X. Yang, Y. Liu, G. Ji, S. Ge, X. Wang, M. Wang, “Lymph node metastasis in cancer progression: molecular mechanisms, clinical significance and therapeutic interventions,” *Sig Transduct Target Ther*, vol. 8, no. 1, p. 367, Sep. 2023, doi: 10.1038/s41392-023-01576-4.

[13] “Cancer in Lymph Nodes May Help Tumors Metastasize - NCI.” Accessed: Apr. 26, 2026. [Online]. Available: https://www.cancer.gov/news-events/cancer-currents-blog/2022/cancer-lymph-nodes-metastasis

[14] K. Dhatchinamoorthy, J. D. Colbert, and K. L. Rock, “Cancer Immune Evasion Through Loss of MHC Class I Antigen Presentation,” *Front Immunol*, vol. 12, p. 636568, 2021, doi: 10.3389/fimmu.2021.636568.

[15] Y. Wang and H. Wang, “Lymph node targeting for immunotherapy,” *Immunooncol Technol*, vol. 20, p. 100395, Jun. 2023, doi: 10.1016/j.iotech.2023.100395.

[16] J. I. Andorko, K. L. Hess, and C. M. Jewell, “Harnessing Biomaterials to Engineer the Lymph Node Microenvironment for Immunity or Tolerance,” *AAPS J*, vol. 17, no. 2, pp. 323–338, Mar. 2015, doi: 10.1208/s12248-014-9708-2.

[17] Y. Dimopoulos, E. Moysi, and C. Petrovas, “The Lymph Node in HIV Pathogenesis,” *Curr HIV/AIDS Rep*, vol. 14, no. 4, pp. 133–140, Aug. 2017, doi: 10.1007/s11904-017-0359-7.

[18] “Chemotherapy: Types & How They Work,” Cleveland Clinic. Accessed: Apr. 26, 2026. [Online]. Available: https://my.clevelandclinic.org/health/treatments/16859-chemotherapy

[19] “How Does Radiation Therapy Work?,” Cleveland Clinic. Accessed: Apr. 26, 2026. [Online]. Available: https://my.clevelandclinic.org/health/treatments/17637-radiation-therapy

[20] “Metastasis: What To Expect When Cancer Spreads,” Cleveland Clinic. Accessed: Apr. 26, 2026. [Online]. Available: https://my.clevelandclinic.org/health/diseases/22213-metastasis-metastatic-cancer

[21] “ASCO Guidelines | ASCO Publications,” American Society of Clinical Oncology. Accessed: Apr. 26, 2026. [Online]. Available: https://ascopubs.org/guidelines

[22] “What Are Advanced and Metastatic Cancers?” Accessed: Apr. 26, 2026. [Online]. Available: https://www.cancer.org/cancer/understanding-cancer/what-is-cancer/advanced-and-metastatic-cancer.html

[23] Guest, “The Hidden Reasons for Cancer Metastasis and Drug Resistance,” NFCR. Accessed: Apr. 26, 2026. [Online]. Available: https://www.nfcr.org/blog/hidden-reasons-cancer-metastasis-drug-resistance/

[24] J. Kim, P. A. Archer, and S. N. Thomas, “Innovations in Lymph Node Targeting Nanocarriers,” *Semin Immunol*, vol. 56, p. 101534, Aug. 2021, doi: 10.1016/j.smim.2021.101534.

[25] N. S. lrvin-Choy, K. M. Nelson, J. P. Gleghorn, and E. S. Day, “Design of nanomaterials for applications in maternal/fetal medicine,” *J Mater Chem B*, vol. 8, no. 31, pp. 6548–6561, Aug. 2020, doi: 10.1039/d0tb00612b.

[26] S. Khan, M. Sharifi, J. P. Gleghorn, M. M. Nejadi Babadaei, et al, “Artificial engineering of the protein corona at bio-nano interfaces for improved cancer-targeted nanotherapy.” *Journal of Controlled Release*, 348, 127-147. 2022. doi:10.1016/j.jconrel.2022.05.055.

[27] P. H. D. Nguyen, M. K. Jayasinghe, A. H. Le, B. Peng, and M. T. N. Le, “Advances in Drug Delivery Systems Based on Red Blood Cells and Their Membrane-Derived Nanoparticles,” *ACS Nano*, vol. 17, no. 6, pp. 5187–5210, Mar. 2023, doi: 10.1021/acsnano.2c11965.

[28] Q. Dai, S. Wilhelm, D. Ding, A. M. Syed, S. Sindhwani, Y. Zhang, Y. Y. Chen, P. MacMilan, W. C. Chan, “Quantifying the Ligand-Coated Nanoparticle Delivery to Cancer Cells in Solid Tumors,” *ACS Nano*, vol. 12, no. 8, pp. 8423–8435, Aug. 2018, doi: 10.1021/acsnano.8b03900.

[29] N. S. Irvin-Choy, K. M. Nelson, M. N. Dang, J. P. Gleghorn, and E. S. Day, "Gold nanoparticle biodistribution in pregnant mice following intravenous administration varies with gestational age," *Nanomedicine*, vol. 36, p. 102412, Aug. 2021, doi: 10.1016/j.nano.2021.102412.

[30] M. Sharifi, W. C. Cho, A. Ansariesfahani, R. Tarharoudi, H. Malekisarvar, S. Sari, S. H. Bloukh, Z. Edis, M. Amin, J. P. Gleghorn, et al, "An Updated Review on EPR-Based Solid Tumor Targeting Nanocarriers for Cancer Treatment." *Cancers*, 14, 2868. 2022. doi:10.3390/cancers14122868.

[31] C. M. Jewell, S. C. Bustamante López, and D. J. Irvine, "In situ engineering of the lymph node microenvironment via intranodal injection of adjuvant-releasing polymer particles," *Proceedings of the National Academy of Sciences*, vol. 108, no. 38, pp. 15745–15750, Sep. 2011, doi: 10.1073/pnas.1105200108.

[32] Z. Fu, S. Li, S. Han, C. Shi, and Y. Zhang, "Antibody drug conjugate: the 'biological missile' for targeted cancer therapy," *Sig Transduct Target Ther*, vol. 7, no. 1, p. 93, Mar. 2022, doi: 10.1038/s41392-022-00947-7.

[33] X. Zhou, Y. Han, Y. Fang, P. Ma, J. Zhou, Y. Jiang, S. Xing, Q. Tang, Y. Hou, S. Wang, N. Li, "Antibody-drug conjugates: Current challenges and innovative solutions for precision cancer therapy," *Med*, vol. 6, no. 10, p. 100849, Oct. 2025, doi: 10.1016/j.medj.2025.100849.

[34] R. E. Young, K. M. Nelson, S. I. Hofbauer, T. Vijayakumar, M. G. Alameh, D. Weissman, C. Papachristou, J. P. Gleghorn, R. S. Riley, "Systematic development of ionizable lipid nanoparticles for placental mRNA delivery using a design of experiments approach." *Bioactive Materials*, 34, 125-137. 2024. doi:10.1016/j.bioactmat.2023.11.014.

[35] K. M. Nelson, N. Irvin-Choy, M. K. Hoffman, J. P. Gleghorn, and E. S. Day, "Diseases and conditions that impact maternal and fetal health and the potential for nanomedicine therapies," *Adv Drug Deliv Rev*, vol. 170, pp. 425–438, Mar. 2021, doi: 10.1016/j.addr.2020.09.013.

[36] W. B. Liechty, D. R. Kryscio, B. V. Slaughter, and N. A. Peppas, "Polymers for drug delivery systems," *Annu Rev Chem Biomol Eng*, vol. 1, pp. 149–173, 2010, doi: 10.1146/annurev-chembioeng-073009-100847.

[37] R. Riahi, A. Tamayol, S. A. M. Shaegh, A. Ghaemmaghami, M. R. Dokmeci, and A. Khademshosseini, "Microfluidics for Advanced Drug Delivery Systems," *Curr Opin Chem Eng*, vol. 7, pp. 101–112, Feb. 2015, doi: 10.1016/j.coche.2014.12.001.

[38] S. E. Alavi *et al.*, "Microfluidics for personalized drug delivery," *Drug Discovery Today*, vol. 29, no. 4, p. 103936, Apr. 2024, doi: 10.1016/j.drudis.2024.103936.

[39] R. J. Wilson, Y. Li, G. Yang, and C.-X. Zhao, "Nanoemulsions for drug delivery," *Particuology*, vol. 64, pp. 85–97, May 2022, doi: 10.1016/j.partic.2021.05.009.

[40] M. Cabodi, N. W. Choi, J. P. Gleghorn, C. S. D. Lee, L. J. Bonassar, and A. D. Stroock, "A microfluidic biomaterial," *J Am Chem Soc*, vol. 127, no. 40, pp. 13788–13789, Oct. 2005, doi: 10.1021/ja054820t.

[41] J. P. Gleghorn, E. D. Pratt, C. Denning, H. Liu, N. H. Bander, S. T. Tagawa, D. M. Nanus, P. Giannakakou, B. J. Kirby, "Capture of circulating tumor cells from whole blood of prostate cancer patients using geometrically enhanced differential immunocapture (GEDI) and a prostate-specific antibody." *Lab on a Chip*, 10, 27-29. 2010. doi:10.1039/b917959c.

[42] E. D. Pratt, C. Huang, B. G. Hawkins, J. P. Gleghorn, and B. J. Kirby, "Rare Cell Capture in Microfluidic Devices," *Chem Eng Sci*, vol. 66, no. 7, pp. 1508–1522, Apr. 2011, doi: 10.1016/j.ces.2010.09.012.

[43] B. J. Kirby, M. Jodari, M. S. Loftus, G. Gakhar, E. D. Pratt, C. Chanel-Vos, J. P. Gleghorn, et al, "Functional characterization of circulating tumor cells with a prostate-cancer-specific microfluidic device." *PLoS ONE*, 7(4), e35976. 2012. doi:10.1371/journal.pone.0035976.

[44] J. P. Smith, A. C. Barbati, S. M. Santana, J. P. Gleghorn, and B. J. Kirby, "Microfluidic Transport in Microdevices for Rare Cell Capture," *Electrophoresis*, vol. 33, no. 21, p. 10.1002/elps.201200263, Nov. 2012, doi: 10.1002/elps.201200263.

[45] E. M. Chandler, C. M. Berglund, J. S. Lee, W. J. Polacheck, J. P. Gleghorn, B. J. Kirby, C. Fischbach, "Stiffness of photocrosslinked RGD-alginate gels regulates adipose progenitor cell behavior." *Biotechnology and Bioengineering,* 108(7), 1683-1692. 2011. doi:10.1002/bit.23079.

[46] C. S. D. Lee, J. P. Gleghorn, N. Won Choi, M. Cabodi, A. D. Stroock, and L. J. Bonassar, "Integration of layered chondrocyte-seeded alginate hydrogel scaffolds," *Biomaterials*, vol. 28, no. 19, pp. 2987–2993, Jul. 2007, doi: 10.1016/j.biomaterials.2007.02.035.

[47] J. J. Ballyns, J. P. Gleghorn, V. Niebrzydowski, J.J. Rawlinson, H. G. Potter, S. A. Maher, T. M. Wright, L. J. Bonassar, "Image-guided tissue engineering of anatomically shaped implants via MRI and micro-CT using injection molding." *Tissue Engineering: Part A*, 14(7), 1195-1202. 2008. doi:10.1089/ten.tea.2007.0186.

[48] M. J. Donzanti, B. J. Ferrick, O. Mhatre, B. Chernokal, D. C. Renteria, and J. P. Gleghorn, "Stochastic to Deterministic: A Straightforward Approach to Create

Serially Perfusable Multiscale Capillary Beds," *ACS Biomater. Sci. Eng.*, vol. 11, no. 1, pp. 239–248, Jan. 2025, doi: 10.1021/acsbiomaterials.4c01247.

[49] A. Amouzegar, M. Chelvanambi, J. N. Filderman, W. J. Storkus, and J. J. Luke, "STING Agonists as Cancer Therapeutics," *Cancers*, vol. 13, no. 11, p. 2695, Jan. 2021, doi: 10.3390/cancers13112695.

[50] K. M. Nelson, B. J. Ferrick, H. Karimi, C. L. Hatem, and J. P. Gleghorn, "A straightforward cell culture insert model to incorporate biochemical and biophysical stromal properties into transplacental transport studies," *Placenta*, vol. 166, pp. 54–61, Jun. 2025, doi: 10.1016/j.placenta.2024.09.001.

[51] N. W. Choi, M. Cabodi, B. Held, J. P. Gleghorn, L. J. Bonassar, A. D. Stroock, "Microfluidic scaffolds for tissue engineering." *Nature Materials*, 6, 908-915. 2007. doi:10.1038/nmat2022.

[52] D. H. Kim, J. E. Cha, D. Kim, and S. H. Lee, "Size-Controlled Fabrication of Alginate Hydrogel Microbeads Optimized for Lipase Entrapment," *Gels*, vol. 11, no. 9, pp. 710–710, Sep. 2025, doi: https://doi.org/10.3390/gels11090710.

[53] N. A. Filatov, D. V. Nozdriukhin, A. A. Evstrapov, and A. S. Bukatin, "Comparison of step and flow-focusing emulsification methods for water-in-oil monodisperse drops in microfluidic chips," *Journal of Physics: Conference Series*, vol. 1124, p. 031028, Dec. 2018, doi: https://doi.org/10.1088/1742-6596/1124/3/031028.

[54] G. Della Rosa, N. E. Gostynska, J. W. Ephraim, S. Sganga, G. Panuccio, G. Palazzo, N. Tirelli, "Magnesium alginate as a low-viscosity (intramolecularly cross-linked) system for the sustained and neuroprotective release of magnesium,"

Carbohydrate Polymers, vol. 331, p. 121871, May 2024, doi: https://doi.org/10.1016/j.carbpol.2024.121871.

[55] H. O. Bahwal, K. Akhtar, W. A. Bawazir, S. H. Alharthi, and S. B. Khan, "Preparation of crosslinked alginate hydrogels for the adsorption and sustainable release of doxorubicin hydrochloride," *Polymers*, vol. 17, no. 24, p. 3294, Dec. 2025. doi:10.3390/polym17243294.

[56] C. T. Pan, S. T. Chen, T. C. Chiang, C. K. Yen, S. Y. Wang, Z. H. Wen, C. Y. Yu, Y. L. Shiue, "Optimization of the spherical integrity for sustained-release alginate microcarriers-encapsulated doxorubicin by the Taguchi method," *Scientific Reports*, vol. 10, no. 1, Dec. 2020. doi:10.1038/s41598-020-78813-1.

[57] F. Briggs, D. Browne, and P. Asuri, "Role of polymer concentration and crosslinking density on release rates of small molecule drugs," *International Journal of Molecular Sciences*, vol. 23, no. 8, p. 4118, Apr. 2022. doi:10.3390/ijms23084118.

[58] K. Tabatabaei, S. Moazzezi, M. Emamgholizadeh, H. Vaez, B. Baradaran, B. Shokouhi, "Improved therapeutic efficacy of doxorubicin chemotherapy with cannabidiol in 4t1 mice breast cancer model," *Cancer Med*, Sep. 2023. doi:10.21203/rs.3.rs-3257947/v1.

[59] R. M. Desai, S. T. Koshy, S. A. Hilderbrand, D. J. Mooney, and N. S. Joshi, "Versatile click alginate hydrogels crosslinked via tetrazine–norbornene chemistry," *Biomaterials*, vol. 50, pp. 30–37, May 2015, doi: https://doi.org/10.1016/j.biomaterials.2015.01.048.

[60] F. Kullenberg, O. Degerstedt, C. Calitz, N. Pavlović, D. Balgoma, J. Gråsjö, E. Sjögren, M. Hedeland, F. Heindryckx, H. Lennernäs., "In Vitro Cell Toxicity and Intracellular Uptake of Doxorubicin Exposed as a Solution or Liposomes: Implications

for Treatment of Hepatocellular Carcinoma," *Cells*, vol. 10, no. 7, pp. 1717–1717, Jul. 2021, doi: https://doi.org/10.3390/cells10071717.

[61] S. Zhou, F. Cheng, Y. Zhang, T. Su, and G. Zhu, "Engineering and Delivery of cGAS-STING Immunomodulators for the Immunotherapy of Cancer and Autoimmune Diseases," *Accounts of chemical research*, vol. 56, no. 21, pp. 2933–2943, Jul. 2023, doi: https://doi.org/10.1021/acs.accounts.3c00394.

[62] S. I. Hofbauer, L.A. Fink, R. E. Young, T. Vijayakumar, K. M Nelson, N. Bellopede, M.G. Alameh, D. Weissman, J. P. Gleghorn, R. S. Riley, "Cytokine mRNA Delivery and Local Immunomodulation in the Placenta Using Lipid Nanoparticles." *Advanced Therapeutics*. 2025. doi:10.1002/adtp.202500148.

[63] W. Wei and P. Lu, "Engineering pH and Temperature-Triggered Drug Release with Metal-Organic Frameworks and Fatty Acids," *Molecules*, vol. 29, no. 22, pp. 5291–5291, Nov. 2024, doi: https://doi.org/10.3390/molecules29225291.

[64] M. J. Donzanti*, Y. Moghadamnia*, A. T. Kapinski, R. Zurakowski, J. P. Gleghorn, "Anatomical 3D Reconstruction of Murine Lymph Nodes for Visualization, Quantitation, and Numerical Simulation." *bioRxiv*. 2025. doi:10.1101/2025.11.25.690560. *Co-first authors.

[65] B. Chernokal, B. J. Ferrick, J. P. Gleghorn, "Zonal patterning of extracellular matrix and stromal cell populations along a perfusable cellular microchannel." 2024. *Lab on a Chip.*

[66] D. J. Minahan, K. M Nelson, F. Ribeiro, B. J. Ferrick, A. M. Zurzolo, K. Byers, V. Mckeown, J. P. Gleghorn, "Democratizing Organ-On-Chip Technologies With a Modular, Reusable, and Perfusion-Ready Microphysiological System." *Advanced Healthcare Materials*, 15(1), e02202. 2025. doi:10.1002/adhm.202502202.

[67] B. J. Ferrick, J. P. Gleghorn, “Modular Parallel Plate Flow Chamber with Tunable Substrate Mechanics and Defined Shear Stress.” *Biomedical Microdevices* (Preprint: bioRxiv 2025.04.30.651503).

[68] V. L. Edwards, E. McComb, J. P. Gleghorn, L. Forney, P. M. Bavoil, J. Ravel, “Three-dimensional models of the cervicovaginal epithelia to study host-microbiome interactions and sexually transmitted infections.” *Pathogens and Disease*, 80, ftac026. 2022. doi:10.1093/femspd/ftac026.

[69] K. M. Nelson, B. J. Ferrick, H. Karimi, C. L. Hatem, J. P. Gleghorn, “A straightforward cell culture insert model to incorporate biochemical and biophysical stromal properties into transplacental transport studies.” *Placenta*. 2024. doi:10.1016/j.placenta.2024.09.001.

[70] K. M. Nelson, D. J. Minahan, V. L. Edwards, I. J. Glomski, D. J. Delgado Diaz, K. Thomas, F. C. Walker, P. M. Bavoil, I. Derre, A. K. Criss, J. Ravel*, J. P. Gleghorn*, “A microphysiologic human cervical model recapitulates microbial, immune, and pathogenic properties of sexually transmitted infections.” *Science Advances*, 12(14), eaeb4864. 2026. doi:10.1126/sciadv.aeb4864. *Co-corresponding authors.

[71] J. Felsenstein, K. M. Nelson, J. Shirazi, J. P. Gleghorn, “Therapeutic nanoparticle safety in pregnancy: Bridging knowledge gaps with environmental insights and a translational roadmap.” *Journal of Controlled Release*. 2025. doi:10.1016/j.jconrel.2025.114026.

[72] L. Hallee, J. P. Gleghorn, “Protein-Protein Interaction Prediction is Achievable with Large Language Models.” *bioRxiv*. 2023. doi:10.1101/2023.02.26.530111.

[73] L. Hallee, T. Peleg, N. Rafailidis, J. P. Gleghorn, “Protein Language Models are Accidental Taxonomists.” *bioRxiv*. 2025. doi:10.1101/2025.10.07.681002.

[74] L. Hallee, R. Kapur, A. Patel, J. P. Gleghorn, B. Khomtchouk, “Contrastive Learning and Mixture of Experts Enables Precise Vector Embeddings (CAMP)”. *Scientific Reports.* 2025.

[75] L. Hallee L, N. Rafailidis, J. P. Gleghorn, “Diffusion Sequence Models for Enhanced Protein Representation and Generation.” bioRxiv/arXiv preprint (NeurIPS 2025 submission). 2024.

[76] L. Hallee, N. Rafailidis, C. Horger, D. Hong, J. P. Gleghorn, “Annotation Vocabulary (Might Be) All You Need.” *bioRxiv*. 2024. doi:10.1101/2024.07.31.605924.

[77] L. Hallee L, J. P. Gleghorn, “Dual Triangle Attention: Effective Bidirectional Attention Without Positional Embeddings.” arXiv preprint, arXiv:2506.06203. 2026.